Eoarchean subduction-like magmatism recorded in ca. 3750 Ma mafic–ultramafic rocks of the Ukaliq supracrustal belt (Québec)

Thomas Grocolas[1], Pierre Bouilhol[1], Guillaume Caro[1], Stephen J. Mojzsis[2]

[1]Université de Lorraine, CNRS, CRPG, 54000 Nancy, France

[2]Department of Geological Sciences, University of Colorado, UCB 399, 2200 Colorado Avenue, Boulder, CO 80309-0399, USA

Key Points:

- We document the preservation of magmatic phases in Eoarchean rocks of the Ukaliq supracrustal belt
- Two liquid lines of descent corresponding to a tholeiitic suite and a boninitic, fluid-saturated suite are identified
- The modeled differentiation sequences coupled with the negative μ^{142}Nd anomalies point to a subduction-like environment

Supporting Information:

Figures S1 to S3

Tables S1 to S3

Correspondence to:

T. Grocolas. Present address: Institute of Earth Sciences, University of Lausanne, 1015 Lausanne, Switzerland. E-mail: thomas.grocolas@unil.ch

Abstract

Our understanding of the nature of crustal formation in the Eoarchean is severely curbed by the scarcity and poor preservation of the oldest rocks, and variable and imperfect preservation of protolith magmatic signatures. These limitations hamper our ability to place quantitative constraints on thermomechanical models for early crustal genesis and hence on the operative geodynamical regimes at that time. Controls on the liquid line of descent responsible for Eoarchean crust petrogenesis could help us understand more, but these remain vague. Growth of Archean crust may have occurred dominantly via processes akin to modern oceanic crustal genesis, coupled to a vertical geodynamic regime. Equally, convergent boundary processes, including subduction, are argued to be important in the development of the crust before about 3.8 Ga. The recently discovered ca. 3.75 Ga Ukaliq supracrustal enclave (northern Québec) is mainly composed of serpentinized ultramafic rocks and amphibolitized mafic schists. Inferred protoliths to the Ukaliq serpentinites include dunites, pyroxenites, and hornblendites with compositions similar to that of arc crust cumulates, whereas the mafic rocks were probably basalts to basaltic andesites. The Ukaliq cumulates record two liquid lines of descent: (i) a tholeiitic suite, partially hydrated, resulting from the fractionation of a basaltic liquid; and (ii) a boninitic suite documenting the evolution of an initially primitive basaltic to andesitic melt at ~0.5 GPa and containing >6 wt% H_2O. Together with the presence of negative μ^{142}Nd anomalies, this information points to a deep fluid input via recycling of Hadean crust in the Eoarchean via modern-style subduction.

Plain Language Summary

The processes of crust formation that prevailed during the first billion year of Earth's history remain largely speculative. Based on numerical modeling, two contrasting views of early Earth's crustal formation have been proposed, involving either a modern-like, plate tectonic

regime or a vertical, non-plate tectonic regime. Deciphering between these geodynamic models require understanding the origin and evolution of Eoarchean magmas, but these remain poorly constrained due to the extreme scarcity and overall poor preservation of Earth's oldest rocks. In this study, we document the petrography of mafic and ultramafic rocks of the recently discovered 3.75 Ga Ukaliq supracrustal belt in northern Québec. We show that the mineralogy and chemistry of the ultramafic rocks are similar to modern subduction-related arc lower crust while mafic rocks are comparable to arc-related lavas. This observation allows defining two magmatic series: (i) a partially hydrous tholeiitic suite; and (ii) a highly hydrated, low pressure boninitic suite. The high water content inferred for the boninitic suite combined with their anomalous ^{142}Nd signature are symptomatic of the recycling of a Hadean lithosphere via modern-style subduction.

1. Introduction

Earth's crust has been sculpted by plate tectonics for billions of years; the process mainly responsible for this complex dynamic is subduction. It is widely held that since its inception, plate tectonics has governed the mode of crust formation and cooling, as well as the long-term operation of the geochemical cycles and, hence, the evolution of the atmosphere, hydrosphere, and biosphere in what has been termed "biogeodynamics" (e.g., Stern, 2002; Von Huene & Scholl, 1991; Zerkle, 2018). Within the plate tectonics milieu, subduction zones generate continental crust through mantle wedge partial melting and magmatic accretion beneath island arcs (Ringwood, 1974; Taylor & McLennan, 1985). The record of Hf isotopes in zircon is interpreted to show that >70% of crustal growth occurred in the Archean, or before about 2.5 Ga (e.g., Belousova et al., 2010; McCulloch & Bennett, 1994). Yet, a petrogenetic process to explain such a crustal growth trajectory remains widely speculative. This is even more so when the question of continental development is paired with various geodynamic models. Based mostly on geochemical and mechanical-structural constraints, the prevailing view asserts that vertical tectonics rather than active subduction molded the Hadean–Archean Earth's crust (e.g., Bédard et al., 2003; Shirey & Richardson, 2011). Considering a mantle potential temperature 300°C greater than that of today, mantle melting should have occurred at a greater depth to produce a thick buoyant crust (Johnson et al., 2014; Korenaga, 2006; McKenzie & Bickle, 1988; Sleep, 2005). Arguably, the thermal and mechanical properties of such thick crust inhibited subduction processes to instead favor emplacement of a long-lived lithosphere susceptible to reworking via what may have been catastrophic vertical transfer (e.g., Bédard, 2006; Bédard, 2018). At odds with these interpretations are recent numerical models which show that plate tectonics can proceed even under the thermal boundary conditions of very thick and buoyant crust (e.g., Maunder et al., 2016; Weller et al., 2019). Shirey et al. (2008) present petrological and geochemical constraints compatible with the initiation of subduction at approximately 3.9 Ga. Similarly, the

composition of the liquid in equilibrium with the Hadean Jack Hills zircons as well as new Si isotopes constraints on Eoarchean tonalites–trondjhemites–granodiorites (TTG) lend support to the idea that the onset of plate tectonics occurred at the Hadean–Eoarchean transition around 4 Ga ago rather than sometime later (Deng et al., 2019; Turner et al., 2020). A competing study of silicate and sulfide inclusions captured in ancient diamonds argues in favor of the initiation of plate tectonics after about 3 Ga (Shirey & Richardson, 2011), whereas other work from studies of ophiolites and high-pressure metamorphic terranes (Stern, 2005) proposes that this process only began as recently as Neoproterozoic time. To resolve these conflicting conclusions about Earth's history of plate tectonics requires analysis of the oldest terranes. The main challenge is to identify Eoarchean crustal remnants that preserve petrological and geochemical characteristics consistent with protolith formation at convergent margin settings under the hydrochemical and thermochemical influences of subduction.

One such ancient terrane is the ~12,000 km^2 Archean Inukjuak domain in the northeast Superior Province of Québec, Canada (Greer et al., 2020). Briefly, the Eoarchean supracrustal enclaves of the Ukaliq (and nearby Nuvvuagittuq) locality are part of the Innuksuac complex (Simard et al., 2003), an association of scattered variably-deformed supracrustal rafts which range in size from <1 m to >1 km and caught up within the granitoid gneisses of the Inukjuak domain. As described elsewhere (Caro et al., 2017), the Ukaliq rocks comprise a series of mafic schists interpreted to have volcanic protoliths chemically similar to those found in a modern forearc environment such as tholeiitic and boninitic lavas. These are also associated with calc-alkaline andesites, the identification of which brings into question the exclusivity of a vertical tectonic model for the entirety of the Archean (e.g., Turner et al., 2014). We wish to emphasize that the Innuksuac complex has parallels with rocks documented in the 3.7–3.81 Ga Isua supracrustal belt (ISB; southern West Greenland; Szilas et al., 2015), as well as in younger Archean complexes (e.g., Cawood et al., 2006). As opposed to the ISB rocks which have well-documented

higher $^{142}Nd/^{144}Nd$ values (Caro et al., 2003) relative to bulk silicate Earth (BSE) and reported in the conventional $\mu^{142}Nd$ notation as positive anomalies, the numerous lithologies of the Innuksuac complex preserve variably negative $\mu^{142}Nd$ anomalies (Caro et al., 2017; O'Neil et al., 2008; Roth et al 2013). There are two ways to explain these divergent $\mu^{142}Nd$ values for what otherwise appears to be synchronous Eoarchean terranes: (i) the negative $\mu^{142}Nd$ were produced by *in situ* decay of ^{146}Sm after emplacement of the rocks, in which case the Nuvvuagittuq belt is of Hadean age (O'Neil et al., 2008, 2019); or (ii) the negative $\mu^{142}Nd$ signature is inherited from a now-vanished Hadean lithosphere and the $\mu^{142}Nd$–Sm/Nd correlation interpreted by O'Neil et al (2008) as an isochron represents a mixing line without any geochronological significance. Such an inherited signal can be duplicated by crustal assimilation or subduction of Hadean crust (Caro et al., 2017).

However, two key observations belie the assimilation argument. The first of these is that in spite of the ubiquitous Hadean crustal signatures there are no zircons of Hadean age in rocks of the Innuksuac complex. This is despite thousands of U–Pb zircon analyses performed on samples of igneous and detrital sedimentary protoliths collected from throughout the terrane (Chowdhury et al., 2020; Greer et al., 2020 and references therein). A second argument lies in the absence of crustal (felsic) contaminants with sufficiently unradiogenic ^{142}Nd signature to account for the $\mu^{142}Nd$ values found in the Nuvvuagittuq supracrustal belt (NSB) mafic rocks (Caro et al., 2017). To account for these observations, we argue here that a scenario where recycling occurred through a subduction process in the Eoarchean neatly explains not only the typical forearc sequence preserved in the Innuksuac supracrustals, but also the trace element concentrations and the enriched ^{142}Nd and ^{143}Nd signatures contained therein.

In this work, we turn our attention to the ultramafic–mafic supracrustal enclave at the Ukaliq locality to describe (1) the preservation of Eoarchean magmatic features, (2) the cumulate–liquid relationship between the ultramafic and mafic rocks, (3) the cumulate assemblages that

formed during the ascent of primitive magmas, and (4) the corresponding liquid line of descent. Based on these observations, we provide an explanation for the chemical evolution of the supracrustal rocks that requires transition from a water-undersaturated tholeiitic regime to a water-rich boninitic sequence. Today, such an evolution corresponds to a subduction initiation environment.

2. Geological setting

The variably-deformed Eoarchean supracrustal enclaves of the dominantly Neoarchean Inukjuak domain (Minto bloc, northeast Superior Province, Canada) principally comprise plutonic and volcano-sedimentary schists; these range in age from 3.5 to 3.8 Ga, and are metamorphosed to the amphibolite facies (0.4 GPa, 640°C; Cates & Mojzsis, 2009; Greer et al. 2020) with local retrogressions. Although less well-known than cognate Eoarchean rocks of the ISB, the ca. 3.75 Ga NSB was the first to show evidence of anomalous depletions in $^{142}Nd/^{144}Nd$ relative to BSE (negative $\mu^{142}Nd$) that seem to correlate to Sm/Nd (O'Neil et al., 2008). The subject of our study is another neighboring body of metamorphosed volcano-sedimentary rocks also displaying this characteristic ^{142}Nd signature: The Ukaliq supracrustal belt (USB) (Caro et al., 2017). The largest of the USB enclaves is a poly-metamorphosed and intensely deformed NNW-trending flat ellipsoidal body of about 100 m × 7 km (Fig. 1) a few kilometers north from the NSB. The USB is composed of three main lithologies: (i) massive amphibolite composed of hornblende- or cummingtonite-rich rocks inferred to have volcanic protoliths; (ii) ultramafic boudins and enclaves, mainly serpentinized; and (iii) intercalated siliceous units comprising layered and strongly tectonized quartz + magnetite ± amphibole ± pyroxene rocks interpreted as banded-iron formations (BIFs), and quartz + biotite schists and massive to banded quartzite (± fuchsite) of detrital origin (Caro et al., 2017; Greer et al., 2020).

Two forms of ultramafic rocks can be distinguished: (i) a thick layer (~30 m) parallel to the massive NNW-dipping foliation; and (ii) lenses structurally intruding amphibolites (Fig. 2A).

175 The contact between ultramafic and mafic rocks is sharp and comports with the foliation (Fig.
176 2B). Several thin (~10 cm) BIF layers occur within the mafic rocks and are parallel to the re-
177 gional structural trend of the USB enclave. The quartzites are mostly located near the eastern
178 contact between USB rocks and encompassing Voizel suite granitoids (Fig. 1). Ultramafic rocks
179 show a compositional gradient ranging from pure serpentinites in the eastern side to a more
180 pyroxene-rich composition in the west. The NSB differs from the USB in the occurrence of the
181 Ca-poor amphibole cummingtonite; it is rare to uncommon at Ukaliq where the amphibole is
182 hornblende as opposed to the NSB where cummingtonite can be the dominant amphibole in
183 amphibolite. Earlier U–Pb TIMS geochronology on detrital zircons recovered from micaschists
184 in the NSB yields an age of 3825 ± 18 Ma (Darling et al., 2013; David et al., 2002) whereas
185 zircons extracted from intrusive trondjhemitic orthogneisses lead to a minimum emplacement
186 age of 3751 ± 10 Ma (Cates & Mojzsis, 2007; Greer et al., 2020). Elsewhere in the NSB, detrital
187 zircons from detrital fuchsitic quartzites and micaschists interpreted to be quartz-pebble con-
188 glomerates provide a maximum age of emplacement for the various volcanic protoliths of ca.
189 3.78 Ga (Cates et al., 2013; Darling et al., 2013). For a review of the geology of the wider
190 region, we refer the reader to the synthesis in Greer et al. (2020).

191 3. Methods

192 Bulk-rock major and trace elements compositions for the 60 samples reported in Table S1 were
193 performed at the SARM facility (CRPG, Nancy). Further *in situ* major element compositions
194 of minerals from a subset of 16 samples (8 ultramafic rocks and 8 mafic rocks) were determined
195 using the Cameca SX100 electron microprobe at GeoRessources laboratory (Université de Lor-
196 raine). The acceleration voltage was 15 keV and beam conditions were 12 nA, counting times
197 were 10 s. Trace elements analyses of clinopyroxenes (cpx), orthopyroxenes (opx), amphiboles
198 (amph), and garnets (grt) were also performed for 6 samples by laser ablation inductively cou-
199 pled plasma mass spectrometry (LA-ICP-MS) at GeoRessources laboratory using a single-

collector, double-focusing, sector field Agilent 7500 ICP-MS system, coupled with a Geolas platform hosting a 193 nm excimer laser (Geolas Pro). The ablation process was conducted in an ablation cell of 30 cm^3 in a He atmosphere, then mixed with Ar before entering the plasma. Acquisition time for blanks and sample analysis was set to 1 min. The laser was used at an energy of 15 J cm^{-2} and a frequency of 10 Hz with a spot size ranging from 60 to 80 μm for cpx, hbl and grt, and from 120 to 150 μm for opx. ^{29}Si was used as an internal standard based on the electron microprobe analyses. Analyte concentrations were calibrated against the NIST 612 rhyolite glass.

4. Structure and petrography

Three main lithologies were identified during our mapping of the main USB body: (i) ultramafic rocks (pyroxene-rich to pure serpentinite) present as enclaves or as a decameter-sized layer; (ii) hornblende- or cummingtonite-bearing amphibolites; and (iii) quartzitic and micaceous rocks of sedimentary protolith with foliation parallel to that expressed in the amphibolites.

4.1. Ultramafic rocks

At the base of the sequence with foliation that strikes N70, ultramafic rocks are dark green massive serpentinite (Fig. 2C). These serpentinites are mainly composed of antigorite (atg) and chlorite (chl). At the microscopic scale, relict opx, amph, and cpx range from <0.1 mm to >2 mm (Figs. 3A to 3D). Anhedral amph form millimeter-sized phenocrysts and are preferentially altered in chl and atg along cleavage planes. Fresh, rounded cpx (<0.1 mm) is present in one sample (IN16098b) as inclusions in hornblende (hbl) or at hbl grain boundaries (Fig. 3D). This sample will hereafter be referred to as a cpx-bearing ultramafic rock. Opx are only present in cpx-absent ultramafic rocks as submillimeter inclusions in amph or as phenocryst in contact with amph. The contact between amph and opx is sharp and points to a relict cumulate texture (Fig. 3B). When opx is present as large crystals (>1 cm), it shows corroded boundaries and atg pseudomorph lamellae perpendicular to cleavage. We interpret these large opx crystals as

remnants of a heteradcumulate texture (Campbell, 1968). Brownish, corroded spinels (spl) occur at amph and opx grain boundaries or as inclusions in these two phases. Within two samples, greenish, millimeter-sized spl is in equilibrium with talc and probably corresponds to late overprinting phases. To summarize, the textural relationships suggest that opx, cpx and amph may represent relics of the magmatic phases, and that atg, chl, talc, and greenish spl are metamorphic overprints.

4.2. Amphibolites

Volumetrically, the USB amphibolites are dominated by a dark, massive unit and many other smaller deformed enclaves of amphibolites and paragneisses scattered throughout the complex (Chowdhury et al., 2020; Greer et al., 2020). At the mesoscale, the mafic rocks display a fine-grained (<0.5 mm) texture with a typical amph + plagioclase (plag) ± cpx ± quartz (qtz) paragenesis (Fig. 2D). Ilmenite and titanite can occur at grain boundaries (<0.1 mm). Rarely, light grey to beige amphibolite occurs within the USB and corresponds to the cummingtonite-rich amphibolite much more widespread throughout the neighboring NSB (David et al., 2002). At the microscopic scale, amphibolites exhibit a typical isogranular texture with a foliation marked by millimeter- to centimeter-sized amph which may be colorless (Mg-hbl), green (hbl, tremolite, cummingtonite) to bluish green (pargasite) (Figs. 3E and 3F). Tremolites often surround and grow on top of Mg-hbl. These overgrowths, as well as the presence of cummingtonite, may be attributed to the metamorphic history of the massif. The Mg-hbl are in equilibrium with millimeter-sized plag partially altered to sericite that shows thin polysynthetic twinning, qtz with undulose extinction and subgrain boundaries that are features characteristic of plastic deformation, and cpx having higher refringence than amph. A few cpx may be corroded by tremolite. These mineral relationships point to a magmatic origin for Mg-hbl and cpx, while tremolite and cummingtonite are of metamorphic origin.

4.3. Rocks of sedimentary protolith

BIFs are mainly composed of alternating bands of Fe-oxides and silicates, which at weathering renders them a characteristic reddish color. Silicate layers (qtz) record a NNW striking foliation that is parallel to the main structural grain of the USB. At the microscale, the BIF Fe-oxides are associated with ol, cpx and amph, interpreted to form through the isochemical transformation of Fe-oxides and qtz during amphibolite facies metamorphism (e.g., Klein, 2005).

Micaschists of probable detrital origin share the common NNW striking foliation. They exhibit a grano-porphyroblastic texture with numerous aluminous phases such as grt and biotite (bt) that can be used as geothermometer. Porphyric grt (~2 mm) containing bt and qtz inclusions is surrounded by often chloritized, prismatic, millimeter-sized bt. Millimeter-sized plag, amph, and qtz with undulose extinction also occur. Pressure and temperature conditions inferred from grt–bt thermometer and grt compositions are 0.3 ± 0.05 GPa and 650 ± 15°C (Fig. S1). This result agrees with the last metamorphic peak conditions experienced by the NSB (0.4 GPa, 640°C; Cates & Mojzsis, 2009; Greer et al., 2020).

5. Bulk-rock chemistry

Major and trace elements concentrations allow us to distinguish between five different protoliths of magmatic origin in the USB. The ultramafic rocks can be divided into two different groups in accordance with their mineralogy, whereas the amphibolites can be separated in three groups based on major and trace element chemistry. The composition and description of the analyzed rocks is provided in Table S2 and S3, respectively.

5.1. Ultramafic rocks

Ultramafic rocks have high X_{Mg} (83.8–91.7) and low SiO_2 concentrations (37–49 wt%) except for one sample (IN14011) with lower X_{Mg} (75.7) (Fig. 4A). These rocks show a wide range of Al_2O_3 contents (0.32–8.48 wt%) associated with a SiO_2/MgO ratio ranging from 1 to 3 suggesting the presence of ol, opx, and cpx in their protolith (Fig. 4B). Bulk CaO contents define two distinct groups: (i) a CaO-poor (0.45–6.03 wt%), cpx-absent group; and (ii) a CaO-rich (11.76–

12.62 wt%), cpx-bearing group. Most ultramafic rocks have high NiO content (0.19–0.30 wt%) suggesting the presence of ol in the protolith (Fig. 4D). Chondrite-normalized rare earth element (REE) patterns show rather flat segments for heavy REE (HREE; $0.82 < Dy_N/Yb_N < 1.29$) and slightly fractionated middle REE (MREE) ($0.31 < Sm_N/Dy_N < 1.80$) (Fig. 5B). Most samples are enriched in light REE (LREE; $0.66 < La_N/Sm_N < 6.27$) and show a variable Eu anomaly ($Eu^* = Eu_N/[Sm_N \times Gd_N]^{1/2}$; Eu* = 0.13–3.12). Normalized to primitive mantle (PM), ultramafic rocks display slight U and Th and strong Cs, Rb, Pb, and K enrichments combined with a pronounced negative Nb anomaly ($Nb^* = Nb_N/[K_N \times La_N]^{1/2}$; 0.06–0.72) (Fig. 5A). A few samples may exhibit negative Zr and Hf anomalies ($Zr^* = Zr_N/[Sm_N \times Nd_N]^{1/2}$), but most have $Zr^* \approx 1$. Ultramafic rocks display Cr contents ranging from 650 to 5000 ppm and are enriched in Sc (7–98 ppm) and depleted in V (2–34 ppm) relative to PM.

5.2. Mafic rocks

Major and trace elements allow distinguishing three main groups of amphibolites in the USB. The first group has average SiO_2 content of about 49 wt% (46.10–53.29 wt%) negatively correlated with X_{Mg} (36.1–69.6; Fig. 4A). Bulk-rock Al_2O_3 ranges from 10.99 to 16.32 wt% except for one sample having lower content (Al_2O_3 = 6.76 wt%). These rocks have high TiO_2 contents (0.72–1.49 wt%; Fig. 4C) resulting in low Al_2O_3/TiO_2 ratios (9–16) as well as high CaO concentrations (6.80–14.12 wt%). Chondrite-normalized REE patterns show flat HREE ($0.97 < Dy_N/Yb_N < 1.23$) and MREE ($0.97 < Sm_N/Dy_N < 1.47$) segments and slightly fractionated LREE ($0.74 < La_N/Sm_N < 1.62$) segment (Fig. 5D). Moreover, a slight positive Eu anomaly may occur in a few samples. These amphibolites are strongly enriched in fluid-mobile elements like Cs, Rb, Pb, and K (Fig. 5C). Besides, these rocks show a broad range of Sr anomalies ($Sr^* = Sr_N/[Ce_N \times Nd_N]^{1/2}$) ranging from 0.27 to 3.57, a negative Nb anomaly (Nb*= 0.15–0.86) and no Zr anomaly. Finally, Cr content (36–276 ppm) is low compared to PM, in contrast to V (25–55 ppm) and Sc (135–362 ppm) concentrations, respectively close and enriched relative to PM.

These amphibolites have major and trace element concentrations characteristics of tholeiitic basalts and will therefore be referred to as tholeiitic amphibolites.

The second group of amphibolites can be distinguished chemically from the tholeiitic amphibolites by their higher X_{Mg} (52.5–72.6), MgO (8.04–18.63 wt%) and SiO_2 concentrations (48.5–52.9 wt%) and lower CaO (0.82–9.34 wt%) and TiO_2 (0.49–0.61 wt%) contents resulting in high Al_2O_3/TiO_2 ratios ranging from 23 to 30 (Figs. 4A and 4C). Chondrite-normalized REE diagram exhibits a U-shaped pattern with a LREE ($1.14 < La_N/Sm_N < 2.73$) and a slightly HREE ($0.81 < Dy_N/Yb_N < 0.98$) enrichment relative to MREE (Fig. 5H). A particularity of these samples lies in their low concentrations of incompatible elements (∑REE = 15.9–22.5 ppm). None of the samples shows a Eu anomaly. Additionally, fluid-mobile elements are strongly enriched in these amphibolites (Fig. 5G). These rocks display a variable Sr anomaly (Sr* = 0.36–2.38), a negative Nb–Ta anomaly (Nb* = 0.08–0.30) and no Zr anomaly (Zr* 0.85–1.17) except for one sample (Zr* = 2.81). Bulk-rock Cr content is higher than tholeiitic amphibolites (438–807 ppm) whereas V (40–56 ppm) and Sc (215–257 ppm) concentrations are similar. Bulk SiO_2 and TiO_2 contents do not satisfy all the conditions to qualify these samples as boninites *s.s.*, but they share many characteristics with modern boninites found in subduction settings (e.g., U-shaped REE pattern; Reagan et al., 2010; Taylor et al., 1994), and will thus be referred to as boninitic amphibolites.

The third group corresponds to transitional amphibolites which have intermediate composition between tholeiitic amphibolites and boninitic amphibolites. They have SiO_2 contents (46.92–52.23 wt%) and X_{Mg} (50.30–76.2) similar to other amphibolite types whereas their CaO content (7.00–10.73 wt%) and Al_2O_3/TiO_2 ratio (12–23) differ from the two previous categories (Fig. 4A). The REE diagrams exhibit a flat HREE segment ($0.95 < Dy_N/Yb_N < 1.15$) coupled with a negative LREE slope ($0.93 < La_N/Sm_N < 2.31$; Fig. 5F). Furthermore, REE concentrations also display a transitional depletion between the boninitic and tholeiitic endmembers (∑REE = 25–

41 ppm). PM-normalized, transitional amphibolites show no Zr anomaly (Zr* = 0.83–1.20) and a strongly negative Nb anomaly (Nb* = 0.11–0.32; Fig. 5E). V (29–48 ppm) and Sc (117–281 ppm) contents are similar to tholeiitic- and boninite-type amphibolites while Cr concentrations represent a transition between these two groups.

Apart from these three groups, one sample (IN12032) has a peculiar chemistry that differs markedly from the other amphibolites. Although its SiO_2 (52.24 wt%) and CaO (8.40 wt%) contents as well as X_{Mg} (52.5) are similar compared to other rocks (Fig. 4A), the Al_2O_3/TiO_2 ratio (27) is as high as boninitic amphibolites. This sample is, however, different from the boninitic amphibolites by higher REE concentrations (∑REE = 52.1 ppm) typified by a strong LREE enrichment (La_N/Sm_N = 4.00) and a HREE depletion compared to N-MORB. When PM-normalized, this sample is depleted in large ion lithophile elements (LILE; $Th_N + U_N$ >30) and exhibits a high field strength elements (HFSE) depletion with a negative Nb–Ta anomaly (Nb* = 0.19; Fig. 5G). Bulk Cr concentration (219 ppm) is lower while V (49 ppm) and Sc (221 ppm) contents are of the same order of magnitude as the other samples.

Finally, these amphibolite groups can also be distinguished on the basis of their isotopic composition. Tholeiitic amphibolites show slightly negative to no μ^{142}Nd anomaly ($-3.4 < \mu^{142}Nd < 0.6$) whereas boninitic and transitional amphibolites exhibit negative anomalies ($-5.4 < \mu^{142}Nd < -3.2$) and IN12032 carries the most negative ^{142}Nd signature ($\mu^{142}Nd = -9.4$; Caro et al., 2017). These isotopic anomalies are negatively correlated with the bulk rock Th/La ratio, implying that the trace element chemistry of USB amphibolites is at least partly reflecting the incorporation of an ancient enriched component during their petrogenesis (Caro et al 2017).

5.3.Magmatic signal preservation

It is evident from the mineralogy and geochemistry that the USB underwent at least one metamorphic episode that reached upper amphibolite facies conditions (0.3 GPa, 650°C) in the same range as that described for last NSB metamorphism (Cates & Mojzsis, 2009). In detail, the

Innuksuac complex experienced at least two metamorphic episodes (3622 ± 46 Ma and 2738 ± 25 Ma) at the amphibolite facies (Cates & Mojzsis, 2007, 2009), and that probably correspond to magmatic intrusions of the Voizel and Boizard suites, respectively (e.g., Greer et al., 2020). These metamorphic events also likely modified the most fluid-mobile element concentrations of the USB rock suites. To assess the degree of preservation of the original magmatic signal, REE, HFSE and LILE concentrations are compared to Zr concentrations (Fig. S2), which is fluid-immobile at amphibolite conditions (e.g., Fraser et al., 1997). Both average LREE and average HREE as well as HFSE define a good correlation with Zr (R^2 >0.80) but LILE are uncorrelated to Zr (R^2 = 0.128). This observation can either be interpreted as a magmatic signal, reflecting variable fluid-mediated LILE enrichments in the protolith, or as a late metamorphic overprint. These processes are not mutually exclusive but cannot be distinguished on the basis of trace and major element chemistry. As such, only REE and HFSE concentrations will be now considered as representative of the magmatic signal and used further.

6. Mineral chemistry

6.1. Ultramafic rocks

The clinopyroxenes from the cpx-bearing group of ultramafic rocks in our study do not show chemical zoning and belong to the diopside–hedenbergite solid-solution. They show moderate X_{Mg} variation delineating a trend of decreasing X_{Mg} (95.5–94.6) with increasing Al_2O_3 (0.62–2.09 wt%; Fig. 6A) and increasing TiO_2 (0.11–0.58 wt%; Figs. 6A and 6C). Chondrite-normalized REE patterns show slightly fractionated HREE ($1.28 < Dy_N/Yb_N < 1.64$), and MREE ($0.97 < Sm_N/Dy_N < 1.47$) segments and moderately fractionated LREE ($0.59 < La_N/Sm_N < 0.89$) segments (Fig. 6E). The TiO_2-rich cpx grains display a positive Eu anomaly whereas the TiO_2-poor cpx have no Eu anomaly. When PM-normalized, cpx show little to no LILE enrichment and no significant HFSE depletion. Li (2.31–3.66 ppm), Zr (4.89–28.05 ppm), Yb (0.11–0.45 ppm), and Th (0.02–0.05 ppm) contents are positively correlated to X_{Mg} (Fig. 7). We interpret the

composition of high-TiO_2, Eu anomaly-bearing cpx as a magmatic signature while the low-TiO_2 cpx probably experienced partial re-equilibration during metamorphism.

Orthopyroxenes from cpx-absent ultramafic rocks have variable Al_2O_3 (1.22–2.16 wt%), Cr_2O_3 (0–0.31 wt%), and TiO_2 (0.01–0.08 wt%) concentrations at constant X_{Mg} (90.2–87.6; Figs. 6B and 6D). Submillimeter-sized opx exhibits lower X_{Mg} (76.7–78.2) that are uncorrelated with Al_2O_3 and Cr_2O_3 contents. Chondrite-normalized, high-X_{Mg} opx have a highly fractionated MREE to HREE pattern, with Sm_N/Yb_N varying from 0.003 to 0.09, and a contrasting negative LREE slope (Fig. 6F). High-X_{Mg} opx define a trend of decreasing X_{Mg} (90.2–87.6) with increasing Li (1.22–3.55 ppm), Zr (0.12–0.72 ppm), Yb (0.011–0.114 ppm), and Th contents likely reflecting the magmatic evolution of the fractionating melts (Fig. 7).

Brownish spl from ultramafic rocks have Cr-Al spl compositions whereas greenish spl compositions are close to the hercynite endmember (Fig. S3). The Cr-Al spl do not show chemical zoning and define a correlation of increasing Cr# [$100 \times Cr/(Cr + Al + Fe^{3+})$; 19.92–49.43] with decreasing X_{Mg} (65.05–40.69). Further, Cr-Al spl inclusions correspond to the higher X_{Mg} values while opx- and hbl-associated spl have lower X_{Mg}, pointing to a magmatic origin. On the other hand, hercynites display low Cr# (5.20–8.78) and high X_{Mg} (48.34–70.80) and are most likely metamorphic.

Amphiboles from cpx-bearing ultramafic rocks are dominantly Mg-hbl and tremolite, the latter forming rims around cpx and Mg-hbl porphyroblasts. The evolution from Mg-hbl core to tremolite rim is sharp, with Si increasing from 7.15 to 7.95 a.p.f.u. while NaK(A) decreases from 0.25 to 0 a.p.f.u. (Fig. 8A). Tremolite represents metamorphic re-equilibration and will not be considered further. Mg-hbl delineate a trend of increasing NaK(A) (0.00–0.35 a.p.f.u.), TiO_2 (0.00–0.89 wt%), and Cr_2O_3 (0.02–0.98 wt%) contents with decreasing X_{Mg} likely recording the chemical evolution of their parental melt (Figs. 8B and 8C). When chondrite-normalized, these Mg-hbl exhibit a nearly parallel pattern compared to cpx except for HREE being less

400 fractionated ($Dy_N/Yb_N \approx 1.20$; Fig. 8D). When PM-normalized, Mg-hbl show slight U, Th, and
401 Pb enrichment and little to no HFSE depletion compared with adjacent elements. Li content
402 ranges from 0.81 to 1.08 ppm (Fig. 7A). Conversely, amph from the cpx-absent group are ex-
403 clusively Mg-hbl with no chemical zoning. They display a trend of increasing TiO_2 concentra-
404 tion with decreasing X_{Mg} whereas low NaK(A) and Cr_2O_3 contents are associated with low X_{Mg}
405 values. Chondrite-normalized, these Mg-hbl have the same U-shaped REE pattern as boninitic
406 amphibolites (Fig. 8D). Normalized to PM, they display strong Nb–Ta negative anomalies and
407 U–Pb enrichments. Moreover, these Mg-hbl are usually more depleted in trace elements than
408 amph from cpx-bearing ultramafic rocks.
409 Antigorite from the cpx-bearing group has high X_{Mg} (89.54–90.94), low Al_2O_3 concentrations
410 (0.84–1.20 wt%), and NiO content ranging from 0.00 to 0.11 wt%. Then again, atg from the
411 cpx-absent group have slightly lower X_{Mg} (87.37–88.27), higher Al_2O_3 (2.44–3.36 wt%) and
412 NiO (0.14–0.15 wt%) content values. We interpret the high Ni atg as most likely ol pseudo-
413 morphs.
414 6.2.Amphibolites
415 Clinopyroxenes from tholeiitic-to-transitional amphibolites have a wide range of X_{Mg} (46.2–
416 73.1) and display a rough trend of decreasing X_{Mg} with increasing Al_2O_3 concentrations (Fig.
417 6A). Al and Ti contents are positively correlated and follow the trend defined by cpx from
418 ultramafic rocks (Fig. 6C). Chondrite-normalized REE patterns show flat HREE ($0.80 <$
419 $Dy_N/Yb_N < 0.95$) and MREE segments ($0.89 < Sm_N/Dy_N < 1.12$) whereas LREE are moderately
420 fractionated ($0.14 < La_N/Sm_N < 0.70$). The cpx displays a negative Eu anomaly and show no
421 enrichment in fluid-mobile elements (Li ≈ 1 ppm; Fig. 7A). Cpx are not present in boninitic
422 amphibolites.
423 Amphiboles from tholeiitic-to-transitional mafic rocks are Mg-hbl, in association with retro-
424 gression tremolite and pargasite (NaK(A) >0.5 a.p.f.u.; Si <6.5 a.p.f.u.). The Mg-hbl and

pargasite display a broad range of X_{Mg} from 36.07 to 84.13 and show a negative correlation with Na_2O while TiO_2 content is uncorrelated with X_{Mg} (Fig. 8B). Chondrite-normalized, the amph exhibit a nearly parallel pattern compared to cpx from mafic rocks, but with higher concentrations, a feature previously documented in magmatic amphiboles derived from melt reacted cpx (e.g., Bouilhol et al., 2015). In one sample (IN14020), amph are MREE- and HREE-depleted ($2.81 < Sm_N/Yb_N < 5.64$) and display high Li content (5.97–10.54 ppm) in comparison with other samples ($1.32 < Li < 2.06$ ppm), which points to a metamorphic origin. Amph from boninitic amphibolites are cummingtonites, which corresponds to CaO-poor (0.40–1.17 wt%) metamorphic amph. These various metamorphic amph will not be further discussed. Overall, cpx and Mg-hbl cores have compositions similar to those found in arc related basalts and andesites (Figs. 6, 7 and 8), and differ from metamorphic phases which usually display Al_2O_3, TiO_2 and Cr_2O_3 depletion (e.g., Zhao et al., 2000) coupled with fluid-mobile elements enrichment (e.g., Li). Furthermore, the required metamorphic conditions to form cpx and opx in mafic lithologies requires upper amphibolite to granulitic facies conditions (Pattison, 2003 and references therein) which have never been reached by USB rocks, supporting a magmatic origin for these minerals.

Plagioclase from tholeiitic-to-transitional amphibolites have compositions ranging from labradorite to andesine with high Ca (0.23–0.71 a.p.f.u.) and Na (0.29–0.73 a.p.f.u.) contents whereas K concentrations (0.00–0.32 a.p.f.u.) are low. The plag from boninitic amphibolites were not analyzed.

7. Discussion

In this section, we use bulk-rock and mineral chemistry to infer the petrogenetic relationship between ultramafic rocks and amphibolites in the Eoarchean Ukaliq supracrustals. By untangling the metamorphic signal from the original magmatic signal, we reconstruct the cumulate

449 sequence followed by tholeiitic and boninitic melts, characterize primary magmas, and by ex-
450 tension, their associated liquid lines of descent.

451 7.1. Protoliths of Ukaliq mafic and ultramafic rocks

452 As shown in previous section, Ukaliq ultramafic rocks display major element concentrations
453 typical of dunite ($SiO_2 \approx 40$ wt%), clinopyroxenite ($SiO_2 \approx 48$ wt%), orthopyroxenite ($SiO_2 \approx$
454 50–52 wt%) and hornblendite ($SiO_2 \approx 40$ wt%; $X_{Mg} \approx 70$). High NiO content and low SiO_2/MgO
455 suggest the presence of cumulative ol in their protolith. Furthermore, opx, cpx and Mg-hbl from
456 ultramafic rocks exhibit a relict magmatic texture as well as compositions that comport with
457 that of cumulates. This is well demonstrated by the bulk-rock X_{Mg} of the ultramafic rocks that
458 range from 72 to 90 whereas the mantle has higher X_{Mg} (~91). The compatible element contents,
459 such as Ni, Cr, and V, also point to a cumulate origin for the ultramafics. Indeed, refractory
460 mantle rocks have Ni contents up to 3000 ppm whereas pyroxenitic cumulates have concentra-
461 tions ranging from 200 to 1400 ppm (e.g., Bodinier and Godard, 2014; Bouilhol et al., 2009,
462 2015). The mineral chemistry also points to a cumulative origin rather than a mantle origin as
463 cpx and opx from USB ultramafic rocks have REE concentrations up to ten times the chondrite
464 values, while cpx from sub-arc mantle and from abyssal peridotites have LREE content values
465 ten to hundred times lower than chondrite (Bodinier and Godard, 2014; Bouilhol et al., 2009).
466 As such, the two identified ultramafic groups (cpx-present and cpx-absent) correspond to two
467 different cumulate suites.

468 Amphibolite samples show basaltic (SiO_2 <52 wt%) to andesitic (SiO_2 >52 wt%) major element
469 compositions with X_{Mg} ranging from 38.17 to 68.11 which cannot be used to distinguish be-
470 tween an intermediate cumulate and a lava. However, these amphibolites show little to no Eu
471 anomaly and have relatively high compatible element contents, which corresponds to volcanic
472 rocks rather than gabbroic cumulates. Indeed, if they were to be gabbroic rocks, Ni and Sc
473 contents would have been much lower than if those amphibolites were to be undifferentiated

lavas, as these elements would have been fractionated in the early stage of gabbro formation. Furthermore, gabbroic rocks usually show a cumulate signal, either cpx-dominated or plag-dominated, resulting in REE pattern with LREE depletion and variable Eu anomaly. Such a signature is not observed in the amphibolites. These observations point to a volcanic rather than a gabbroic protolith for USB amphibolites. Specifically, we interpret the protoliths of the cpx-bearing, TiO_2-rich amphibolites as tholeiitic basalts and the protoliths of the opx-bearing, TiO_2-poor amphibolites as boninitic basalts to andesites

7.2.Relationship between ultramafic cumulates and lavas

Structural and mineralogical evidences suggest that the ultramafic cumulates and the basaltic lavas are cogenetic. Indeed, amphibolites and ultramafic rocks share an intimate relationship, whereby the cumulates are always included in the amphibolites suggesting that their respective protolith were spatially related. Petrologically, the ultramafic cumulates and mafic lavas can be subdivided in two groups with a cpx-bearing suite and a cpx-absent suite. In order to demonstrate the cogenetic character of the cpx-bearing cumulates and tholeiitic(-to-transitional) lavas on one hand, and the cpx-absent cumulates and boninitic lavas on the other, we calculated the REE concentrations of the melts in equilibrium with cpx and opx in the two different cumulate series. The parental melt calculated for cpx from cpx-bearing cumulates has a X_{Mg} of 70.81 and show a REE pattern similar to that observed in transitional basalts, albeit with slightly lower HREE concentrations (Fig. 9A). As the calculated melt has a X_{Mg} of ~70, whereas the transitional basalts have lower X_{Mg} (50–60), such HREE discrepancy can be alleviated by fractionation. As such, the cumulative cpx could represent an early cumulative phase of the transitional suite. The calculated liquid in equilibrium with magmatic opx from cpx-absent ultramafic cumulates is slightly depleted in MREE compared to the LREE and HREE, reproducing the typical U-shaped pattern observed in boninitic melts (Fig. 9B). Compared to USB boninitic amphibolites, the calculated melt shows a more pronounced depletion in MREE. However, as the

calculated melt has a X_{Mg} of ~75, while the boninitic basalts have a lower X_{Mg} (55–65), a few percent of fractionation could explain such a disparity. We therefore interpret the cpx-bearing ultramafic rocks as cumulate products of tholeiitic-to-transitional basalts and the cpx-absent ultramafic rocks as cumulates of the boninitic basalts.

7.3. Primitive melts and liquid lines of descent

Most amphibolites have characteristics of liquids, and some of them have chemical attributes of primitive liquids that can be primary melts in equilibrium with mantle ol (X_{Mg} = 87–91; Ni = 1800–4500 ppm) and Cr-spl. With respect to partition coefficients (Roeder and Emslie, 1970) and Fe^{3+}/Fe_{tot} uncertainties, the most primitive amphibolites that have melt-like compositions with X_{Mg} = 60–75, MgO >8 wt%, Ni = 120–500 ppm, and Cr ≤1200 ppm are now considered as primitive melts. The most primitive tholeiitic melt has X_{Mg} = 60, SiO_2 = 46.51 wt%, Ni = 394 ppm, and Cr = 356 ppm (Fig. 10A). The primitive boninitic melt displays a X_{Mg} of 68, SiO_2 = 50.35 wt%, Ni = 162 ppm, and Cr = 807 ppm (Fig. 10C). These primitive melts can be considered as the parental liquids of two distinct differentiation series and used to model the evolution of these series.

Tholeiitic(-to-transitional) and boninitic liquids SiO_2, X_{Mg} and REE variations are modeled following the method of Jagoutz (2010). The model is based on fixed cumulate compositions subtraction rather than mineral–liquid partition coefficients to avoid partition coefficient evolution during differentiation and allowing major element modeling. Parental liquid, cumulate and fractionation-derived liquid compositions are related by Eq. 1:

$$C_{l_n} = \frac{C_{l_{n-1}} - (X \times C_c)}{1 - X} \quad (1)$$

Where C_{l_n} represents SiO_2, X_{Mg} and REE concentrations in the fractionated melt at step n, $C_{l_{n-1}}$ at step $n–1$, and C_c is the cumulate concentrations. Fractionation step is 1% and is defined by Eq. 2:

$$X = \frac{X_{m-1} - X_m}{X_{m-1}} \quad (2)$$

Where X_m is the percentage of melt remaining at step m, and X_{m-1} at step $m–1$. C_c has been constrained using USB bulk cumulate compositions for major elements fractionation and USB mineral chemistry for the REE differentiation model, and C_{l_0} is represented by the tholeiitic and boninitic primitive melts previously defined.

7.3.1. Tholeiitic(-to-transitional) sequence

Sample IN16098b represents the only cpx-bearing ultramafic rock in our sample collection. Nevertheless, and as discussed above, the primitive parental melt probably crystallized ol as the liquidus phase, followed by cpx leading to the formation of dunite and (ol-)clinopyroxenite. This observation contrasts with the ISB cumulates sequence where no cpx has been observed nor inferred from the bulk-rock compositions (Szilas et al., 2015). Ol and cpx fractionation induced an enrichment of SiO_2, Al_2O_3, TiO_2, Li and REE coupled with a rapid X_{Mg} decrease in the residual melt as well as in the more evolved cpx. Around 20% of fractionation is sufficient to reach a basaltic composition (Fig. 10A). Lower Cr content in mafic lavas probably illustrates spl crystallization in the cumulate sequence, although the latter was not observed in thin section. The appearance of hbl leads to the formation of hbl-pyroxenite and hornblendite ($X_{Mg} \approx 70$, $SiO_2 \approx 42$ wt%) and marks a turning-point with a strong SiO_2 increase in the liquid. With continuous differentiation, Mg-hbl becomes more Na-, Ti-, and HREE-rich, reflecting enrichment of these elements in the residual melt (Fig. 10B). Both Cpx and Mg-hbl chemistry show little to no LILE-rich, HFSE-poor fluid signatures. Fractionation of ol, cpx, and Mg-hbl is symptomatic of a partially hydrous, tholeiitic(-to-transitional) liquid line of descent whose ol crystallization as the liquidus phase constrains a pressure as high as 0.7 GPa coupled with an unsaturated water content (H_2O = 3 wt%) (Nandedkar et al., 2014). Furthermore, positive Eu anomaly in Mg-hbl suggests that plag and amphibole did not form simultaneously. Lower Al_2O_3 content in cpx from mafic lavas is thus probably related to the early fractionation of plag ($Al_2O_3 \approx 30$ wt%) as no grt signature has been documented in these rocks. The potential crystallization of

549 plag, modeled using hbl-gabbro compositions from arc middle crust (Bouilhol et al., 2015;
550 Daczko et al., 2012; Greene et al., 2006), would involve a strong SiO_2 enrichment as well as an
551 Al_2O_3 and Na_2O decrease in the residual liquid. Subsequently, the melt followed a path allowing
552 fractionation of ol + cpx + hbl ± plag. Finally, the most evolved andesitic compositions of the
553 tholeiitic suite can be reproduced from a primitive melt undergoing 60% fractionation. The
554 fractionation sequence described above has been applied to the liquid in equilibrium with cpx
555 from tholeiitic-to-transitional cumulate. The results (Fig. 9A) show that 30% fractionation of
556 cpx would allow the liquid to reach transitional melt compositions. The proposed cogenetic
557 character of the tholeiitic(-to-transitional) cumulates and the tholeiitic(-to-transitional) basalts
558 is thus confirmed both by partition coefficient and cumulate phase chemistry modeling.

559 7.3.2. Boninitic sequence

560 As discussed above, ol is probably the first phase to appear at the liquidus. Textural observa-
561 tions suggest that the primitive parental liquid did not form dunite but rather ol-orthopyroxenite
562 whose fractionation yields a rapid X_{Mg} decrease (X_{Mg} <60) coupled to Zr and Li increase at
563 constant SiO_2 content ($SiO_2 \approx 50$ wt%) in the residual liquid (Fig. 10C). Moreover, the opx
564 fractionation enhanced the REE, and especially the LREE, concentrations. Low-X_{Mg} opx dis-
565 playing lower Cr_2O_3 and Al_2O_3 contents suggest Cr-Al spl fractionation initiating during opx
566 crystallization. Subsequent Mg-hbl fractionation is documented by amph surrounding opx and
567 leads to hbl-orthopyroxenite to hornblendite crystallization after ~30% fractionation, which is
568 characteristic of silica-rich primitive melts (e.g., Grove et al., 2002). Fractionation experiments
569 on high X_{Mg} andesites and modern boninites suggest that crystallization started at ~0.5 GPa (Fig.
570 6) and, that the parental primitive melt contained >4 wt% H_2O (Van der Laan, 1989; Kraw-
571 czynski et al., 2012). At this pressure, amph is expected to fractionate at about 1000°C and H_2O
572 $\approx$ 4.5 wt%, and the resulting amph-saturated melts become fluid-saturated at 980°C and $H_2O \approx$
573 6.5 wt% (Foden and Green, 1992). The appearance of Nb and Ta negative anomalies, the

presence of U and Th enrichment, and the LREE enrichment (especially La and Ce) in opx and Mg-hbl indicate that fluids play a key role in the genesis and evolution of the melt. Furthermore, hbl from boninitic cumulates have lower REE contents than hbl from tholeiitic(-to-transitional) cumulates probably hence supporting the hypothesis of a more depleted mantle source.

With increasing differentiation, hbl become Na-, Ti-, and REE-rich, reflecting the progressive enrichment of these elements in the melt (Fig. 10D). Plag crystallization and/or fractionation, yet not observed, may be deduced from Mg-hbl displaying a negative Eu anomaly, and from bulk-rock compositions of the most evolved boninitic liquids suggesting that plag may form and lead to hbl-norite-type cumulate. To model the plag fractionation, we used compositions of arc middle crust hbl-norite from Talkeetna (Greene et al., 2006), Fiordland (Daczko et al., 2012), and Kohistan (Bouilhol et al., 2015) which are in good agreement with this differentiation sequence. Our results show that less than 5% fractionation of hbl-norite would allow the liquid to reach andesitic composition (SiO_2 >52 wt%) at constant X_{Mg}. Finally, boninitic melt compositions are best explained by subsequent 40–50% fractionation of subsequent ol + spl + opx + hbl ± plag. Applying this fractionation sequence to the liquid in equilibrium with opx from boninitic cumulates shows that 30% fractionation of opx would allow the liquid to reach boninitic melt REE compositions (Fig. 9B). Thus, both the partition coefficients and mineral–bulk-rock chemistry methods substantiate the cogenetic character of the boninitic cumulates and the boninitic lavas.

7.4. Eoarchean subduction?

Overall, we demonstrated that USB ultramafic rocks represent the cumulates of the mafic lavas in which they are sequentially a part. We have shown that this complex formed following two liquid lines of descent, one from a H_2O-undersaturated basaltic primitive liquid, and the other from a boninitic primitive melt, that are ubiquitous and best produced during low pressure mantle melting in subduction systems. Tholeiitic(-to-transitional) melts were derived from a near-

599 primitive mantle while boninitic melts were extracted from a highly refractory mantle over-
600 printed by a LREE-enriched component carrying a crustal ^{142,143}Nd signature (Caro et al., 2017).
601 The combined petrological, geochemical and isotopic observations point towards melting of a
602 metasomatized mantle rather than crustal assimilation, to explain the widespread occurrence of
603 boninite-like amphibolite in the Innuksuac complex. This further imply that the isotopic signa-
604 tures recorded in Innuksuac rocks reflects recycling rather than reworking of Hadean crust. Our
605 observations thus provide a unique view of a magmatic system associated with the recycling of
606 the Hadean lithosphere in the mantle, shedding new light on Eoarchean geodynamics, which
607 otherwise strongly rely on thermomechanical and analog modeling studies (e.g., Sizova et al.,
608 2010; Van Hunen and Van den Berg, 2008). Based on these models, two contrasting views are
609 provided which nevertheless are supported by the incomplete geological record of the Archean
610 Earth. They are: (i) the active subduction model (e.g., Van Hunen and Moyen, 2012); and (ii)
611 the stagnant lid model dominated by episodes of mantle overturns (e.g., Bédard, 2018). We
612 emphasize that both models satisfy our observations herein, as they can reproduce petrological
613 processes that would lead to the types of liquids and differentiation series in the Ukaliq supra-
614 crustals. In the subduction model, slab induced corner flow leads to H_2O-assisted decompres-
615 sion melting that generates tholeiitic melts. Harzburgitic residue can further melt in a forearc
616 position at low pressure, in fluid-saturated conditions to yield boninitic melts (Grove et al.,
617 2002; Schmidt and Jagoutz, 2017). These two melting regimes can be juxtaposed in a forearc
618 sequence and are thought to represent subduction initiation as has been proposed for the nearby
619 Nuvvuagittuq belt (Turner et al., 2014). Conversely, in the stagnant lid model, it has been pro-
620 posed that crust imbrication against strong continental fragments may trigger similar petroge-
621 netic environments (overriding plate rifting and melt generation via fluid flux; Bédard, 2018).
622 Going beyond these two scenarios, however, our combined isotopic analyses point to subduc-
623 tion. Indeed, transitional and boninitic rocks from the USB preserve ubiquitous ^{142,143}Nd

negative anomalies attributable to Hadean crust (Caro et al., 2017). Models of crustal growth involving crustal imbrication in a stagnant lid regime (Bédard, 2018) would likely result in the preservation of Hadean lithospheric fragments carrying the ^{142}Nd anomaly, which is not observed in the general area of the Innukjuak domain. A simpler way to explain the ubiquitous presence of Hadean geochemical crustal signature in absence of relict Hadean crustal components is to recycle this ancient lithosphere through subduction. The devolatilization of a ^{142}Nd anomaly-bearing slab would then imprint the mantle wedge and its melt derivatives via fluids carrying the ^{142,143}Nd and HFSE-depleted signatures. Finally, petrological and geochemical features, coupled with isotopic studies, suggest that Eoarchean ultramafic and mafic rocks from USB result from two differentiation sequences in a subduction-like environment ultimately induced by the recycling of a 4.4 Gyr-old lithosphere into the mantle. This suite of interpretations would not be possible without the identification of primary magmatic signatures carried by the Eoarchean rocks of the Ukaliq locality.

8. Conclusions

The Eoarchean (ca. 3.75-3.78 Ga) Ukaliq supracrustal belt is part of the Innuksuac complex within the ca. 12,000 km^2 Inukjuak domain of Québec, Canada. The Ukaliq supracrustals host mafic and ultramafic rocks which can be subdivided in five categories according to their phase relationships and bulk-rock chemistry: (i) tholeiitic basalts; (ii) boninitic basalts to andesites exhibiting TiO_2 depletion and U-shaped REE pattern; (iii) transitional basalts representing a continuum between the two previous categories; (iv) cpx-bearing, tholeiitic(-to-transitional) cumulates; and (v) cpx-absent, boninitic cumulates. We showed through bulk-rock and mineral analyses coupled with melt composition calculations, that the ultramafic rocks represent cumulate products of the mafic lavas and used these data to model a fluid-undersaturated, tholeiitic liquid line of descent consisting of ol + cpx + hbl ± plag fractionation, and a fluid-saturated, boninitic differentiation sequence that crystallized ol + spl + opx + hbl ± plag. The liquid lines

649 of descent inferred from both bulk-rock and mineral chemistry suggest that the Eoarchean
650 Ukaliq supracrustals originated in an environment that was capable of reproducing today's sub-
651 duction zone petrological processes, and thus confirms a subduction origin of the observed
652 ^{142,143}Nd isotopic anomalies.
653
654 **Acknowledgments**
655 This work was supported by the Programme National de Planétologie (PNP) of CNRS/INSU,
656 co-funded by CNES, and by OTELO grant JC/2018. Permissions for fieldwork and sample
657 collection were granted through the Pituvik Landholding Corporation and the Pituvik Corpora-
658 tion of Nunavik (Québec), and in particular to the indispensable assistance and advice provided
659 by General Manager Mr. Mike Carroll. Fieldwork was supported by funding from the Agence
660 Nationale de la Recherche (Grant ANR-11-JS56-0012 "DESIR"), and by the Collaborative for
661 Research in Origins (CRiO) directed by S.J.M. and supported by The John Templeton Founda-
662 tion (principal investigator: S. Benner/FfAME/Award #54466): the opinions expressed in this
663 publication are those of the authors, and do not necessarily reflect the views of the John Tem-
664 pleton Foundation. The NASA Exobiology Program (Grant 09-EXOB09-0123,
665 NNH09ZDA001N-EXOB Investigating the Hadean Earth) supported this work from 2009 to
666 2012. S.J.M. also extends a special thanks to the University of Lorraine and CNRS-CRPG
667 (Nancy, France) for a Visiting Professor appointment during significant phases of the prepara-
668 tion of this manuscript. These ideas contained herein were clarified by discussions and debates
669 with W. Bleeker, J. O'Neil, R. Carlson and D. Francis. We also thank Elizabeth Bell, Fannie
670 Thibon, Sarah Davey, Martin Guitreau, Jonathan Oulton, Antoine Roth and Dustin Trail for
671 valuable discussions and assistance in the fieldwork.
672
673 **Figure captions**

Fig. 1. Geological map of the southernmost Ukaliq supracrustal belt and sample localization. Samples whose $^{146,147}Sm$–$^{142,143}Nd$ data are available are represented as well as U–Pb ages for Voizel and Boizard suites. Modified after Caro et al. (2017).

Fig. 2. Ultramafic and mafic rock associations within the Ukaliq supracrustal belt. (A) Ultramafic rocks and amphibolites outcrop exhibiting a subvertical contact or an enclave relationship (N58°18.542', W77°41.487'). (B) Sharp contact between amphibolite and ultramafic rocks showing an orange to brownish alteration color. (C) Ultramafic rock sample (IN14023) displaying a dark greenish color associated with high serpentinization (N58°18.559', W77°41.490'). (D) Photograph of the widespread amph + plag paragenesis of amphibolites (IN14004; N58°18.682', W77°41,547').

Fig. 3. Photomicrographs in cross-polarized light (A, B, D and F) and plane-polarized light (C and E) illustrating mineralogy and textural features of USB rocks. Abbreviations as in the text. (A) Ultramafic sample exhibiting amph in contact with ol inclusion-bearing opx porphyroblast. (B) Spl inclusions in opx and amph porphyroblasts within an ultramafic rock. (C) Spl inclusion-bearing opx porphyroblasts displaying a typical alteration texture within ultramafic rocks. (D) Submillimetric cpx inclusions in amph porphyroblasts being surrounded by atg and chl, representing >70% of ultramafic rocks modal abundance. (E) Mafic rocks exhibiting a granoblastic texture associated with amph + cpx + qtz paragenesis. (F) Fractured centimetric cpx in contact with amph + qtz within a mafic rock.

Fig. 4. Major elements bulk-rock data of USB rocks. Abbreviations as in the text. (A) SiO_2 (wt%) vs. X_{Mg}. (B) Al_2O_3 (wt%) vs. SiO_2/MgO. Ol, opx, cpx, grt, and peridotite fields (Bodinier and Godard, 2014) are represented to infer the protolith type of these poly-metamorphic ultramafic rocks. (C) TiO_2 (wt%) vs. X_{Mg}. (D) NiO vs. X_{Mg}. N-MORB, arc basalts and andesites compositions from Kelemen et al. (2003) are shown for comparison.

Fig. 5. Bulk-rock chondrite-normalized REE, and PM-normalized trace elements contents. (A), (B) Ultramafic rocks. (C), (D) Tholeiitic basalts compared to N-MORB and the average boninitic basalts composition. (E), (F) Transitional basalts compositions compared to N-MORB and the average boninitic basalts composition. (G), (H) Boninitic and calc-alkaline basalts. N-MORB concentrations are represented as comparison. Normalized values are from Sun and McDonough (1989) and McDonough and Sun (1995).

Fig. 6. Major and trace element compositions of cpx (A, C, E) and opx (B, D, F). Abbreviations as in the text. (A) Al_2O_3 (wt%) vs. X_{Mg}. (B) Al_2O_3 (wt%) vs. X_{Mg}. (C) Al_2O_3 (wt%) vs. TiO_2. (D) Cr_2O_3 (wt%) vs. X_{Mg}. (E) Cpx chondrite-normalized REE pattern from ultramafic and mafic rocks. (F) Opx chondrite-normalized REE pattern from ultramafic rocks. Magmatic and metamorphic pyroxenes from Bouilhol et al. (2015) and Zhao et al. (2000) are shown for comparison. Fractionation experiments conducted at various pressures and using different starting materials (Grove et al., 2003; Krawczynski et al., 2012; Nandedkar et al., 2014; Ulmer et al., 2018) are also represented. Normalization values are from Sun and McDonough (1989).

Fig. 7. Trace elements compositions of cpx, opx and amph. Abbreviations as in the text. (A) Li (ppm) vs. X_{Mg}. High Li contents are from sample IN14020. (B) Zr (ppm) vs. X_{Mg}. Mineral compositions from modern arc lower crust are from Bouilhol et al. (2015).

Fig. 8. Major and trace element compositions of amph. Abbreviations as in the text. (A) Leake classification diagram of amph. Structural formulas are recalculated assuming no Na on the M4 site. Tremolite and cummingtonite are represented as pale shaded symbols. (B) TiO_2 (wt%) vs. X_{Mg} for Mg-hbl and pargasite. (C) Cr_2O_3 (wt%) vs. X_{Mg} for Mg-hbl and pargasite. (D) Mg-hbl chondrite-normalized REE pattern from ultramafic and mafic rocks. Magmatic and metamorphic Mg-hbl are shown as comparison and are from Bouilhol et al. (2015) and Zhao et al. (2000), respectively. Fractionation experiments conducted at various pressures and using different starting materials (Grove et al., 2003; Krawczynski et al., 2012; Nandedkar et al., 2014;

Ulmer et al., 2018) are also represented. Normalization values are from Sun and McDonough (1989).

Fig. 9. Trace element compositions of (A) cpx and (B) opx and their calculated parental melts using the partition coefficients of Wood and Blundy (1997) and Bédard (2007) respectively. The green and brown arrays represent the USB transitional basalts and boninitic basalts compositions, respectively. Normalization values are from Sun and McDonough (1989).

Fig. 10. Results of the fractionation model for the tholeiitic suite (A) and the boninitic suite (B) contents. Abbreviations as in the text. (A) SiO_2 (wt%) vs. X_{Mg}. The black lines and the grey fields illustrate the liquid lines of descent calculated following the described model and the cumulate lines of descent, respectively. Crosses indicate a 10% fractionation step. The larger triangle symbols illustrate the fractionated cumulate composition and the smaller triangle symbols represent the measured USB bulk-rock compositions. Hbl-gabbro and hbl-norite compositions are from Greene et al. (2006), Daczko et al. (2012) and Bouilhol et al. (2015).

Fig. 11. Geodynamical model accounting for both the petrological and geochemical characteristics of the Ukaliq supracrustal belt. Legend as in previous figures. The negative ^{142}Nd anomalies in boninitic basalts to andesites (Caro et al., 2017) are reproduced through melting or dehydration of a recycled Hadean crust that transfers its isotopic signature to the overlying mantle. Tholeiitic(-to-transitional) and boninitic primitive lavas are generated through partial melting of the mantle wedge, carrying the $\mu^{142}Nd$ anomalies to the Eoarchean crust. Fractionation starts in the lower crust for the tholeiitic(-to-transitional) and boninitic liquids and continues at shallower depths until andesitic compositions are reached.

Data Availability Statement

Datasets for this research are included in the EarthChem data repository (https://doi.org/10.26022/IEDA/111745).

748

749 **References**

750 Bédard, J. H., Brouillette, P., Madore, L. & Berclaz, A. (2003). Archaean cratonization and
751 deformation in the northern Superior Province, Canada: An evaluation of plate tectonic versus
752 vertical tectonic models. *Precambrian Research*, *127*, 61–87. https://doi.org/10.1016/S0301-
753 9268(03)00181-5

754 Bédard, J. H. (2006). A catalytic delamination-driven model for coupled genesis of Archaean
755 crust and sub-continental lithospheric mantle. *Geochimica et Cosmochimica Acta*, *70*(5), 1188–
756 1214. https://doi.org/10.1016/j.gca.2005.11.008

757 Bédard, J. H. (2007). Trace element partitioning coefficients between silicate melts and ortho-
758 pyroxene: parameterizations of D variations. *Chemical Geology*, *244*, 263–303.
759 https://doi.org/10.1016/j.chemgeo.2007.06.019

760 Bédard, J. H. (2018). Stagnant lids and mantle overturns: Implications for Archaean tectonics,
761 magmagenesis, crustal growth, mantle evolution, and the start of plate tectonics. *Geoscience*
762 *Frontiers*, *9*(1), 19–49. https://doi.org/10.1016/j.gsf.2017.01.005

763 Belousova, E. A., Kostitsyn, Y. A., Griffin, W. L., Begg, G. C., O'Reilly, S. Y. & Pearson, N.
764 J. (2010). The growth of the continental crust: constraints from zircon Hf-isotope data. *Li-*
765 *thos*, *119*(3-4), 457–466. https://doi.org/10.1016/j.lithos.2010.07.024

766 Bodinier, J. L. & Godard, M. (2014). Orogenic, ophiolitic, and abyssal peridotites. *Treatise on*
767 *Geochemistry*, *3*, 103–167. https://doi.org/10.1016/B0-08-043751-6/02004-1

768 Bouilhol, P., Burg, J. P., Bodinier, J. L., Schmidt, M. W., Dawood, H. & Hussain, S. (2009).
769 Magma and fluid percolation in arc to forearc mantle: Evidence from Sapat (Kohistan, Northern
770 Pakistan). *Lithos*, *107*, 17–37. https://doi.org/10.1016/j.lithos.2008.07.004

771 Bouilhol, P., Schmidt, M. W. & Burg, J. P. (2015). Magma transfer and evolution in channels
772 within the arc crust: The pyroxenitic feeder pipes of Sapat (Kohistan, Pakistan). *Journal of Pe-*
773 *trology*, *56*(7), 1309–1342. https://doi.org/10.1093/petrology/egv037
774 Campbell, I. H. (1968). The origin of heteradcumulate and adcumulate textures in the Jimber-
775 lana Norite. *Geological Magazine*, *105*(4), 378–383.
776 https://doi.org/10.1017/S0016756800054431
777 Caro, G., Bourdon, B., Birck, J. L. & Moorbath, S. (2003). ^{146}Sm–^{142}Nd evidence from Isua
778 metamorphosed sediments for early differentiation of the Earth's mantle. *Nature*, *423*, 428–
779 432. https://doi.org/10.1038/nature01668
780 Caro, G., Morino, P., Mojzsis, S. J., Cates, N. L. & Bleeker, W. (2017). Sluggish Hadean geo-
781 dynamics: Evidence from coupled ^{146,147}Sm–^{142,143}Nd systematics in Eoarchean supracrustal
782 rocks of the Inukjuak domain (Québec). *Earth and Planetary Science Letters*, *457*, 23–37.
783 https://doi.org/10.1016/j.epsl.2016.09.051
784 Cates, N. L. & Mojzsis, S. J. (2007). Pre-3750 Ma supracrustal rocks from the Nuvvuagittuq
785 supracrustal belt, northern Québec. *Earth and Planetary Science Letters*, *255*, 9–21.
786 https://doi.org/10.1016/j.epsl.2006.11.034
787 Cates, N. L. & Mojzsis, S. J. (2009). Metamorphic zircon, trace elements and Neoarchean met-
788 amorphism in the ca. 3.75 Ga Nuvvuagittuq supracrustal belt, Québec (Canada). *Chemical Ge-*
789 *ology*, *261*, 99–114. https://doi.org/10.1016/j.chemgeo.2009.01.023
790 Cates, N. L., Ziegler, K., Schmitt, A. K. & Mojzsis, S. J. (2013). Reduced, reused and recycled:
791 Detrital zircons define a maximum age for the Eoarchean (ca. 3750–3780) Nuvvuagittuq su-
792 pracrustal belt, Québec (Canada). *Earth and Planetary Science Letters*, *362*, 283–293.
793 https://doi.org/10.1016/j.epsl.2012.11.054
794 Cawood, P. A., Kroner, A. & Pisarevsky, S. (2006). Precambrian plate tectonics: Criteria and
795 evidence. *Geological Society of America Bulletin*, *16*(7), 4–11.

796 Chowdhury, W., Trail, D., Guitreau, M., Bell, E. A., Buettner, J. & Mojzsis, S. J. (2020). Ge-
797 ochemical and textural investigation of the Eoarchean Ukaliq supracrustals, Northern Québec
798 (Canada). *Lithos*, *372*, 1–20. https://doi.org/10.1016/j.lithos.2020.105673
799 Daczko, N. R., Emami, S., Allibone, A. H. & Turnbull, I. M. (2012). Petrogenesis and geo-
800 chemical characterisation of ultramafic cumulate rocks from Hawes Head, Fiordland, New Zea-
801 land. *New Zealand Journal of Geology and Geophysics*, *55*, 361–374.
802 https://doi.org/10.1080/00288306.2012.719910
803 Darling, J. R., Moser, D. E., Heaman, L. M., Davis, W. J., O'Neil, J. & Carlson, R. (2013).
804 Eoarchean to Neoarchean evolution of the Nuvvuagittuq supracrustal belt: New insights from
805 U–Pb zircon geochronology. *American Journal of Science*, *313*, 844–876.
806 https://doi.org/10.2475/09.2013.02
807 David, J., Parent, M., Stevenson, R., Nadeau, P. & Godin, L. (2002). *La séquence supracrustale*
808 *de Porpoise Cove, région d'Inukjuak; Un exemple unique de croûte paléo-archéenne (ca. 3.8*
809 *Ga) dans la Province du Supérieur*. Ministère des Ressources naturelles et de la Faune (pp. 10–
810 17), Québec, DV.
811 Deng, Z., Chaussidon, M., Guitreau, M., Puchtel, I. S., Dauphas, N. & Moynier, F. (2019). An
812 oceanic subduction origin for Archaean granitoids revealed by silicon isotopes. *Nature Geosci-*
813 *ence*, *12*(9), 774–778. https://doi.org/10.1038/s41561-019-0407-6
814 Foden, J. D. & Green, D. H. (1992). Possible role of amphibole in the origin of andesite: some
815 experimental and natural evidence. *Contributions to Mineralogy and Petrology*, *109*, 479–493.
816 https://doi.org/10.1007/BF00306551
817 Fraser, G., Ellis, D. & Eggins, S. (1997). Zirconium abundance in granulite-facies minerals,
818 with implications for zircon geochronology in high-grade rocks. *Geology*, *25*, 607–610.

819 Greene, A. R., DeBari, S. M., Kelemen, P. B., Blusztajn, J. & Clift, P. D. (2006). A detailed
820 geochemical study of island arc crust: the Talkeetna arc section, South–Central Alaska. *Journal*
821 *of Petrology*, *47*, 1051–1093. https://doi.org/10.1093/petrology/egl002
822 Greer, J., Caro, G., Cates, N. L., Tropper, P., Bleeker, W., Kelly, N. M. & Mojzsis, S. J. (2020).
823 Widespread poly-metamorphosed Archean granitoid gneisses and supracrustal enclaves of the
824 southern Inukjuak Domain, Québec (Canada). *Lithos*, *364*, 1–19. https://doi.org/10.1016/j.li-
825 thos.2020.105520
826 Grove, T. L., Parman, S. W., Bowring, S. A., Price, R. C. & Baker, M. B. (2002). The role of
827 an H_2O-rich fluid component in the generation of primitive basaltic andesites and andesites
828 from the Mt. Shasta region, N California. *Contributions to Mineralogy and Petrology*, *142*,
829 375–396. https://doi.org/10.1007/s004100100299
830 Grove, T. L., Elkins-Tanton, L. T., Parman, S. W., Chatterjee, N., Müntener, O. & Gaetani, G.
831 A. (2003). Fractional crystallization and mantle-melting controls on calc-alkaline differentia-
832 tion trends. *Contributions to Mineralogy and Petrology*, *145*(5), 515–533.
833 https://doi.org/10.1007/s00410-003-0448-z
834 Jagoutz, O. (2010). Construction of the granitoid crust of an island arc. Part II: A quantitative
835 petrogenetic model. *Contributions to Mineralogy and Petrology*, *160*(3), 359–381.
836 https://doi.org/10.1007/s00410-009-0482-6
837 Johnson, T. E., Brown, M., Kaus, B. J. & Van Tongeren, J. A. (2014). Delamination and recy-
838 cling of Archaean crust caused by gravitational instabilities. *Nature Geoscience*, *7*(1), 47–52.
839 https://doi.org/10.1038/ngeo2019
840 Kelemen, P. B., Hanghøj, K. & Greene, A. R. (2003). One view of the geochemistry of sub-
841 duction-related magmatic arcs, with an emphasis on primitive andesite and lower crust. *Treatise*
842 *on Geochemistry*, *3*, 593–659. https://doi.org/10.1016/B0-08-043751-6/03035-8

Klein, C. (2005). Some Precambrian banded iron-formations (BIFs) from around the world: Their age, geologic setting, mineralogy, metamorphism, geochemistry, and origins. *American Mineralogist*, *90*(10), 1473–1499. https://doi.org/10.2138/am.2005.1871

Korenaga, J. (2006). Archean geodynamics and the thermal evolution of Earth. *Geophysical Monograph – American Geophysical Union*, *164*, 7–32. https://doi.org/10.1029/164GM03

Krawczynski, M. J., Grove, T. L. & Behrens, H. (2012). Amphibole stability in primitive arc magmas: effects of temperature, H_2O content, and oxygen fugacity. *Contributions to Mineralogy and Petrology*, *164*(2), 317–339. https://doi.org/10.1007/s00410-012-0740-x

Maunder, B., Van Hunen, J., Magni, V. & Bouilhol, P. (2016). Relamination of mafic subducting crust throughout Earth's history. *Earth and Planetary Science Letters*, *449*, 206–216. https://doi.org/10.1016/j.epsl.2016.05.042

McCulloch, M. T. & Bennett, V. C. (1994). Progressive growth of the Earth's continental crust and depleted mantle: geochemical constraints. *Geochimica et Cosmochimica Acta*, *58*(21), 4717–4738. https://doi.org/10.1016/0016-7037(94)90203-8

McDonough, W. F. & Sun, S. S. (1995). The composition of the Earth. *Chemical geology*, *120*, 223–253. https://doi.org/10.1016/0009-2541(94)00140-4

McKenzie, D. A. N. & Bickle, M. J. (1988). The volume and composition of melt generated by extension of the lithosphere. *Journal of Petrology*, *29*, 625–679. https://doi.org/10.1093/petrology/29.3.625

Nandedkar, R. H., Ulmer, P. & Müntener, O. (2014). Fractional crystallization of primitive, hydrous arc magmas: An experimental study at 0.7 GPa. *Contributions to Mineralogy and Petrology*, *167*(6), 10–15. https://doi.org/10.1007/s00410-014-1015-5

O'Neil, J., Carlson, R. W., Francis, D. & Stevenson, R. K. (2008). Neodymium-142 evidence for Hadean mafic crust. *Science*, *321*, 1828–1831. https://doi.org/10.1126/science.1161925

O'Neil, J., Carlson, R. W., Papineau, D., Levine, Y. E. & Francis, D. (2019). The Nuvvuagittuq greenstone belt: A glimpse of Earth's earliest crust. In: *Earth's Oldest Rocks*, 2nd Edition (pp. 349–374), Elsevier, Amsterdam, Netherlands. https://doi.org/10.1016/B978-0-444-63901-1.00016-2

Pattison, D. R. M. (2003). Petrogenetic significance of orthopyroxene-free garnet + clinopyroxene + plagioclase ± quartz-bearing metabasites with respect to the amphibolite and granulite facies. *Journal of Metamorphic Geology*, *21*, 21–34. https://doi.org/10.1046/j.1525-1314.2003.00415.x

Reagan, M. K., Ishizuka, O., Stern, R. J., Kelley, K. A., Ohara, Y., Blichert-Toft, J., et al. (2010). Fore-arc basalts and subduction initiation in the Izu-Bonin-Mariana system. *Geochemistry, Geophysics, Geosystems*, *11*(3), 1–17. https://doi.org/10.1029/2009GC002871

Ringwood, A. E. (1974). The petrological evolution of island arc systems: Twenty-seventh William Smith Lecture. *Journal of the Geological Society*, *130*(3), 183–204. https://doi.org/10.1144/gsjgs.130.3.0183

Roeder, P. L. & Emslie, R. F. (1970). Olivine–liquid equilibrium. *Contributions to Mineralogy and Petrology*, *29*, 275–289. https://doi.org/10.1007/BF00371276

Roth, A. S., Bourdon, B., Mojzsis, S. J., Touboul, M., Sprung, P., Guitreau, M. & Blichert-Toft, J. (2013). Inherited ^{142}Nd anomalies in Eoarchean protoliths. *Earth and Planetary Science Letters*, *361*, 50–57. https://doi.org/10.1016/j.epsl.2012.11.023

Schmidt, M. W. & Jagoutz, O. (2017). The global systematics of primitive arc melts. *Geochemistry, Geophysics, Geosystems*, *18*, 2817–2854. https://doi.org/10.1002/2016GC006699

Shirey, S. B., Kamber, B. S., Whitehouse, M. J., Mueller, P. A. & Basu, A. R. (2008). A review of the isotopic and trace element evidence for mantle and crustal processes in the Hadean and Archean: Implications for the onset of plate tectonic subduction. In: Condie, K. C. & Pease, V.

(Eds). *When did plate tectonics begin on planet Earth?* Geological Society of America, Special Papers, 440, 1–29. https://doi.org/10.1130/2008.2440(01)

Shirey, S. B. & Richardson, S. H. (2011). Start of the Wilson cycle at 3 Ga shown by diamonds from subcontinental mantle. *Science*, *333*, 434–436. https://doi.org/10.1126/science.1206275

Simard, M., Parent, M., David, J. & Sharma, K. N. M. (2003). *Géologie de la région de la rivière Innuksuac (SNRC 34K et 34L)*. Ministère des Ressources Naturelles (pp. 1–44), Québec, RG.

Sizova, E., Gerya, T., Brown, M. & Perchuk, L. L. (2010). Subduction styles in the Precambrian: Insight from numerical experiments. *Lithos*, *116*, 209–229. https://doi.org/10.1016/j.lithos.2009.05.028

Sleep, N. H. (2005). Evolution of the continental lithosphere. *Annual Review of Earth and Planetary Sciences*, *33*, 369–393. https://doi.org/10.1146/annurev.earth.33.092203.122643

Stern, R. J. (2002). Subduction zones. *Reviews of Geophysics*, *40*(4), 1–42. https://doi.org/10.1029/2001RG000108

Stern, R. J. (2005). Evidence from ophiolites, blueschists, and ultrahigh-pressure metamorphic terranes that the modern episode of subduction tectonics began in Neoproterozoic time. *Geology*, *33*(7), 557–560. https://doi.org/10.1130/G21365.1

Sun, S. S. & McDonough, W. F. (1989). Chemical and isotopic systematics of oceanic basalts: Implications for mantle composition and processes. *Geological Society of London Special Publications*, *42*(1), 313–345. https://doi.org/10.1144/GSL.SP.1989.042.01.19

Szilas, K., Kelemen, P. B. & Rosing, M. T. (2015). The petrogenesis of ultramafic rocks in the >3.7 Ga Isua supracrustal belt, southern West Greenland: Geochemical evidence for two distinct magmatic cumulate trends. *Gondwana Research*, *28*, 565–580. https://doi.org/10.1016/j.gr.2014.07.010

915 Taylor, S. R. & McLennan, S. M. (1985). *The continental crust: Its composition and evolution*.
916 Blackwell, Oxford, 312 pp.
917 Taylor, R. N., Nesbitt, R. W., Vidal, P., Harmon, R. S., Auvray, B. & Croudace, I. W. (1994).
918 Mineralogy, chemistry, and genesis of the boninite series volcanics, Chichijima, Bonin Islands,
919 Japan. *Journal of Petrology*, *35*, 577–617. https://doi.org/10.1093/petrology/35.3.577
920 Turner, S., Rushmer, T., Reagan, M. & Moyen, J. F. (2014). Heading down early on? Start of
921 subduction on Earth. *Geology*, *42*(2), 139–142. https://doi.org/10.1130/G34886.1
922 Turner, S., Wilde, S., Wörner, G., Schaefer, B. & Lai, Y. J. (2020). An andesitic source for Jack
923 Hills zircon supports onset of plate tectonics in the Hadean. *Nature communications*, *11*(1), 1–
924 5. https://doi.org/10.1038/s41467-020-14857-1
925 Ulmer, P., Kaegi, R. & Müntener, O. (2018). Experimentally derived intermediate to silica-rich
926 arc magmas by fractional and equilibrium crystallization at 1.0 GPa: An evaluation of phase
927 relationships, compositions, liquid lines of descent and oxygen fugacity. *Journal of Petrol-*
928 *ogy*, *59*(1), 11–58. https://doi.org/10.1093/petrology/egy017
929 Van der Laan, S. R. (1989). Experimental evidence for the origin of boninites: Near-liquidus
930 phase relations to 7.5 kbar. In: *Boninites and Related Rocks* (pp. 113–147), Unwin Hyman,
931 London.
932 Van Hunen, J. & Van den Berg, A. P. (2008). Plate tectonics on the early Earth: Limitations
933 imposed by strength and buoyancy of subducted lithosphere. *Lithos*, *103*, 217–235.
934 https://doi.org/10.1016/j.lithos.2007.09.016
935 Van Hunen, J. & Moyen, J. F. (2012). Archean subduction: fact or fiction? *Annual Review of*
936 *Earth and Planetary Sciences*, *40*, 195–219. https://doi.org/10.1146/annurev-earth-042711-
937 105255

938 Von Huene, R. & Scholl, D. W. (1991). Observations at convergent margins concerning sedi-
939 ment subduction, subduction erosion, and the growth of continental crust. *Reviews of Geophys-*
940 *ics*, *29*(3), 279–316. https://doi.org/10.1029/91RG00969
941 Weller, O. M., Copley, A., Miller, W. G. R., Palin, R. M. & Dyck, B. (2019). The relationship
942 between mantle potential temperature and oceanic lithosphere buoyancy. *Earth and Planetary*
943 *Science Letters*, *518*, 86–99. https://doi.org/10.1016/j.epsl.2019.05.005
944 Wood, B. J. & Blundy, J. D. (1997). A predictive model for rare earth element partitioning
945 between clinopyroxene and anhydrous silicate melt. *Contributions to Mineralogy and Petrol-*
946 *ogy*, *129*, 166–181. https://doi.org/10.1007/s004100050330
947 Zerkle, A. L. (2018). Biogeodynamics: bridging the gap between surface and deep Earth pro-
948 cesses. *Philosophical Transactions of the Royal Society A: Mathematical, Physical and Engi-*
949 *neering Sciences*, *376*, 1–11. https://doi.org/10.1098/rsta.2017.0401
950 Zhao, G., Cawood, P. A., Wilde, S. A., Sun, M. & Lu, L. (2000). Metamorphism of basement
951 rocks in the Central Zone of the North China Craton: Implications for Paleoproterozoic tectonic
952 evolution. *Precambrian Research*, *103*, 55–88. https://doi.org/10.1016/S0301-9268(00)00076-
953 0
954

955 **References from the Supporting Information**

956 Barnes, S. J. & Roeder, P. L. (2001). The range of spinel compositions in terrestrial mafic and
957 ultramafic rocks. *Journal of Petrology*, *42*, 2279–2302. https://doi.org/10.1093/petrol-
958 ogy/42.12.2279

Figure 1.

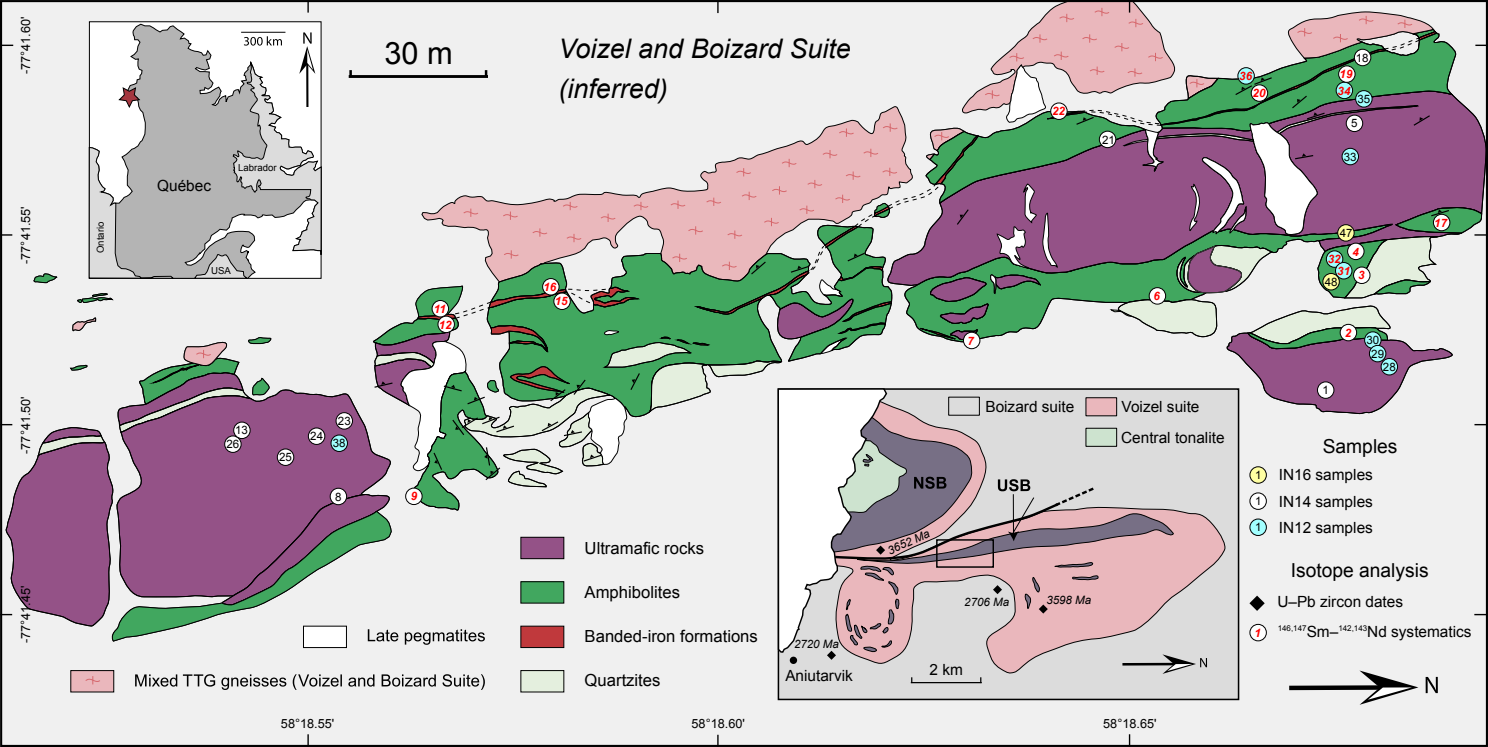
30 m
Voizel and Boizard Suite
(inferred)
300 km
N
Québec
Labrador
Ontario
USA
-77°41.60'
-77°41.55'
-77°41.50'
-77°41.45'
58°18.55'
58°18.60'
58°18.65'
Boizard suite
Voizel suite
Central tonalite
NSB
USB
3652 Ma
2706 Ma
3598 Ma
2720 Ma
Aniutarvik
2 km
N
Ultramafic rocks
Amphibolites
Banded-iron formations
Quartzites
Late pegmatites
Mixed TTG gneisses (Voizel and Boizard Suite)
Samples
IN16 samples
IN14 samples
IN12 samples
Isotope analysis
U–Pb zircon dates
146,147Sm–142,143Nd systematics
N

Figure 2.

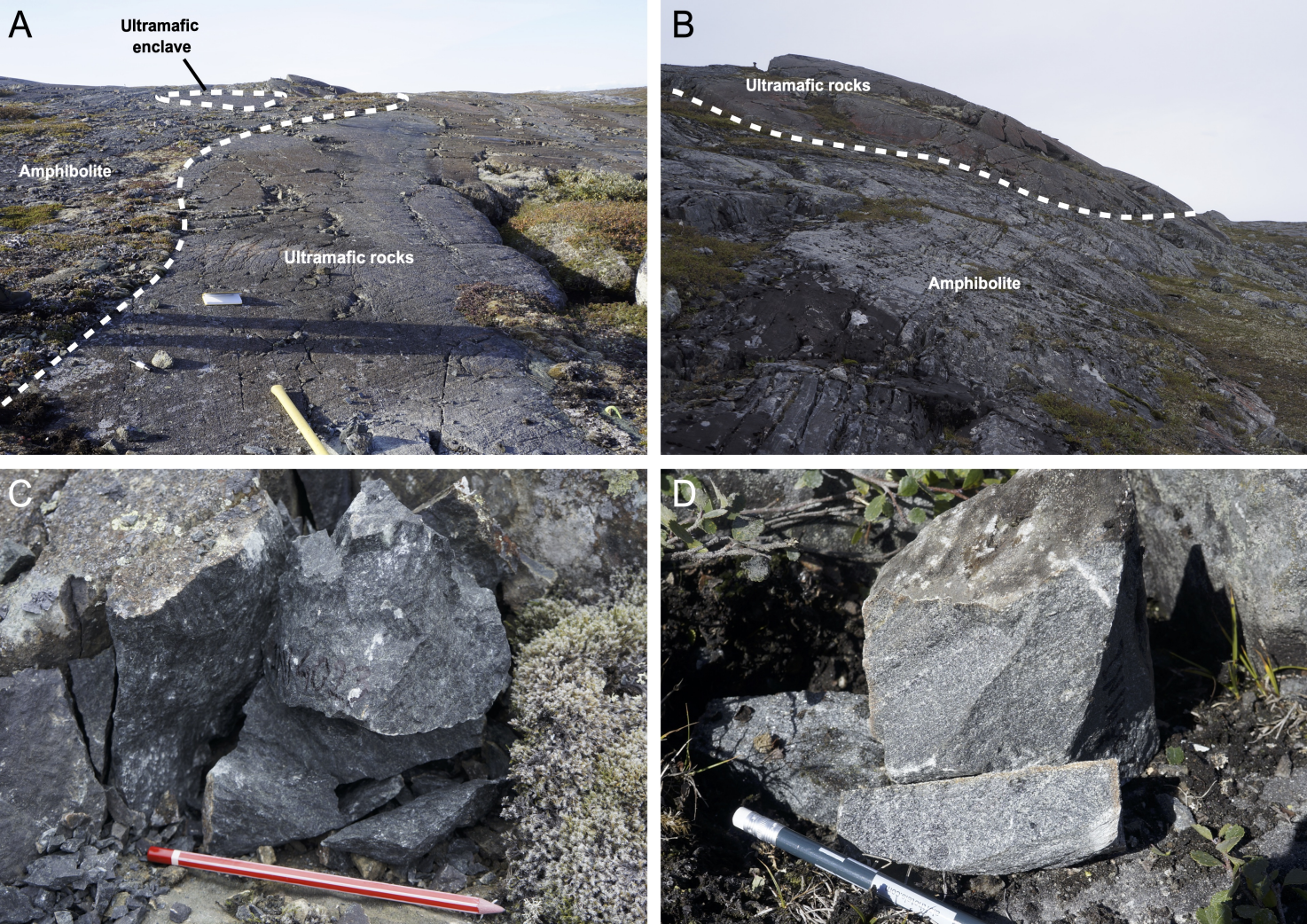
A
Ultramafic enclave
Amphibolite
Ultramafic rocks
B
Ultramafic rocks
Amphibolite
C
D

Figure 3.

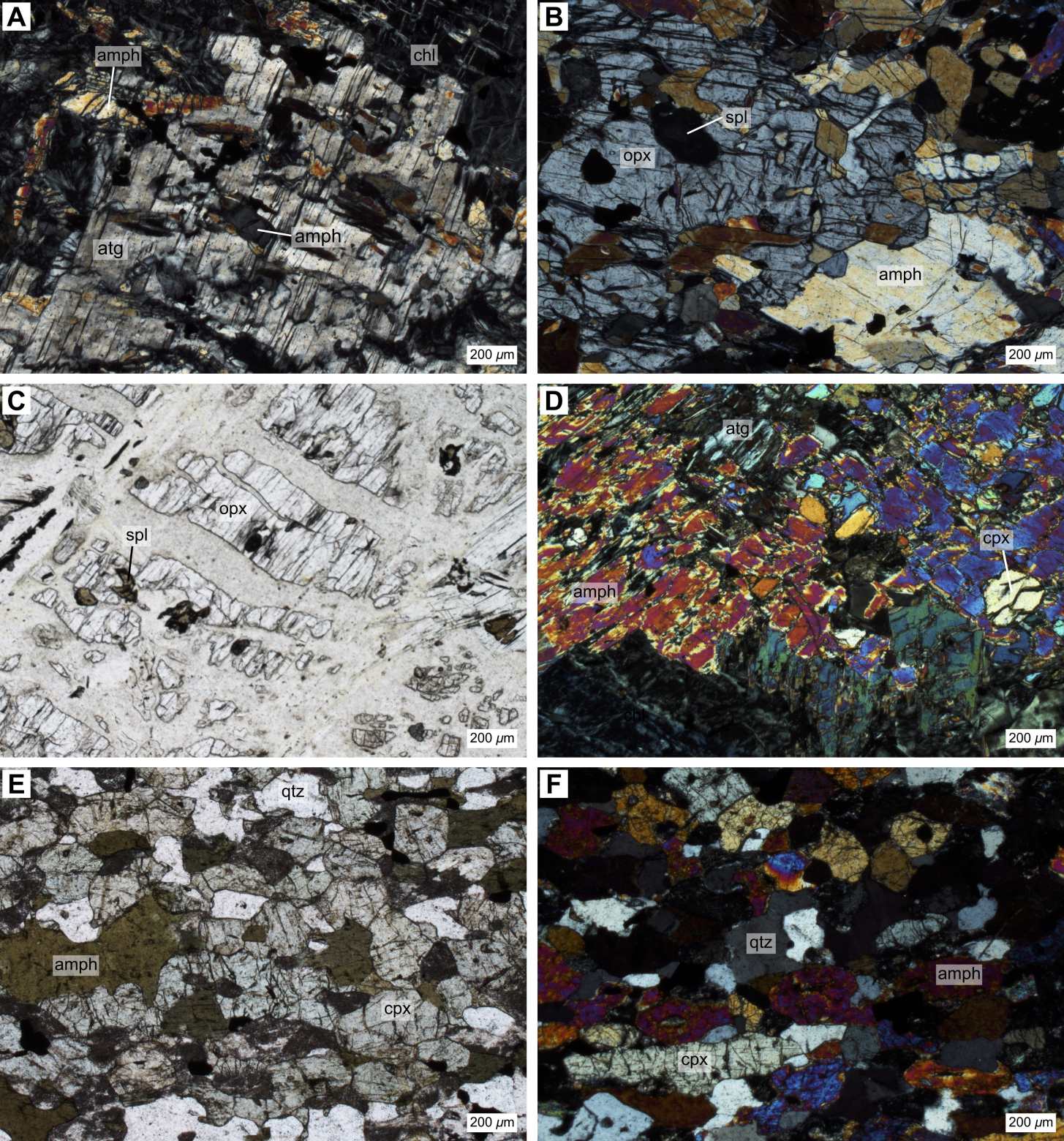
A
amph
chl
atg
amph
200 μm
B
spl
opx
amph
200 μm
C
opx
spl
200 μm
D
atg
cpx
amph
chl
200 μm
E
qtz
amph
cpx
200 μm
F
qtz
amph
cpx
200 μm

Figure 4.

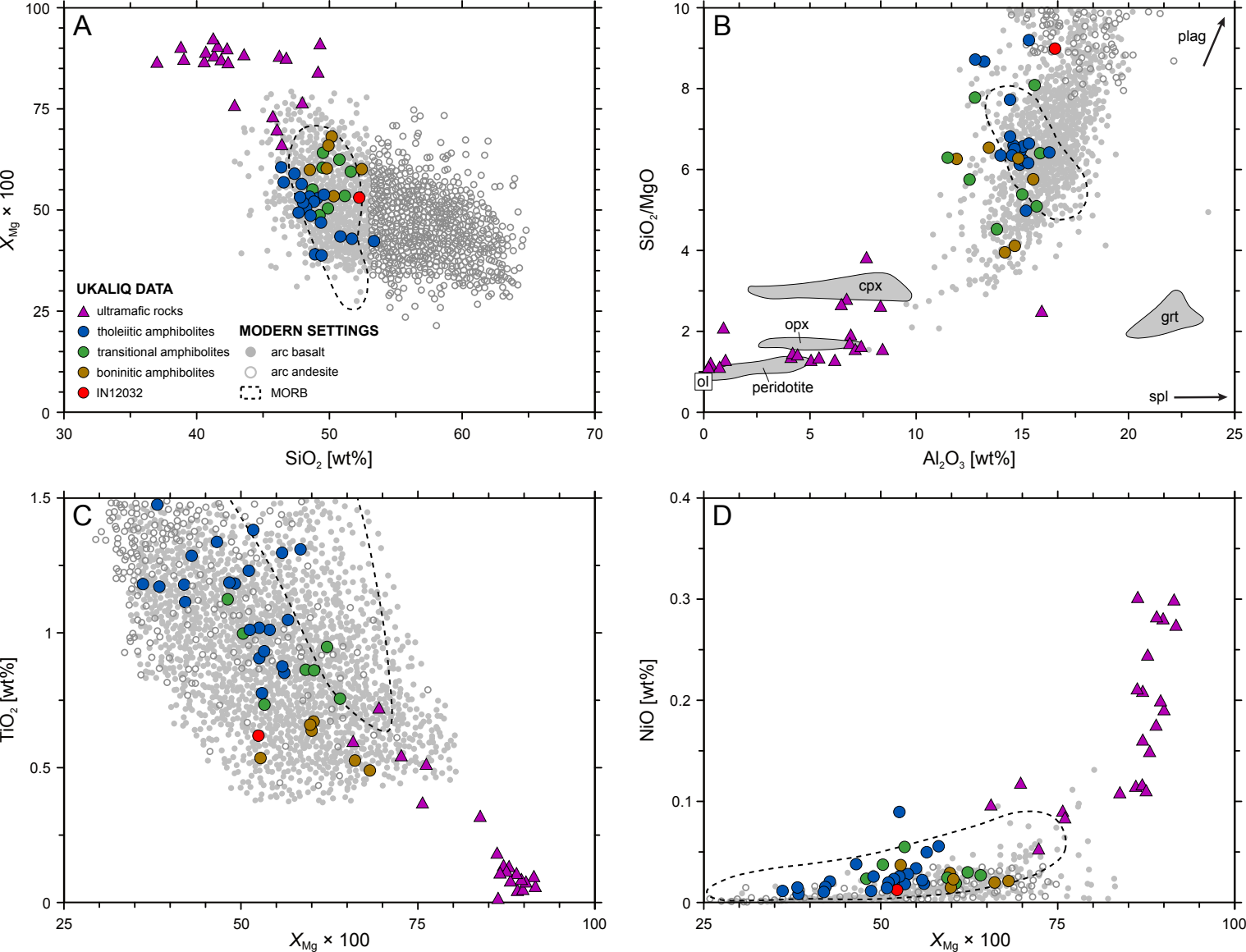
A
B
C
D
UKALIQ DATA
ultramafic rocks
tholeiitic amphibolites
transitional amphibolites
boninitic amphibolites
IN12032
MODERN SETTINGS
arc basalt
arc andesite
MORB
plag
cpx
opx
ol
peridotite
grt
spl
X_{Mg} × 100
SiO_2 [wt%]
SiO_2/MgO
Al_2O_3 [wt%]
TiO_2 [wt%]
NiO [wt%]

Figure 5.

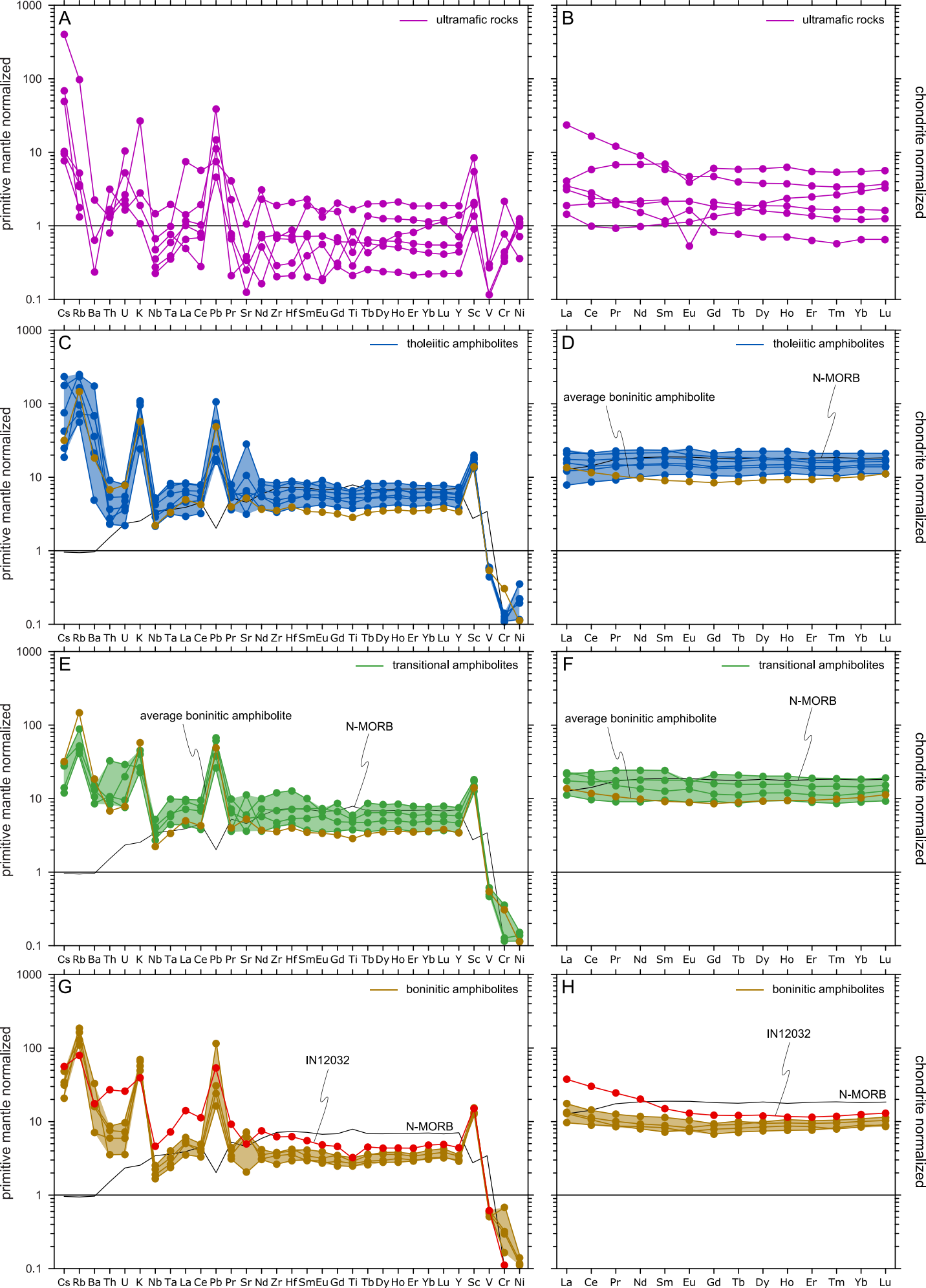
A
ultramafic rocks
B
ultramafic rocks
C
tholeiitic amphibolites
D
tholeiitic amphibolites
average boninitic amphibolite
N-MORB
E
transitional amphibolites
average boninitic amphibolite
N-MORB
F
transitional amphibolites
average boninitic amphibolite
N-MORB
G
boninitic amphibolites
IN12032
N-MORB
H
boninitic amphibolites
IN12032
N-MORB
primitive mantle normalized
chondrite normalized
1000
100
10
1
0.1
Cs Rb Ba Th U K Nb Ta La Ce Pb Pr Sr Nd Zr Hf Sm Eu Gd Ti Tb Dy Ho Er Yb Lu Y Sc V Cr Ni
La Ce Pr Nd Sm Eu Gd Tb Dy Ho Er Tm Yb Lu

Figure 6.

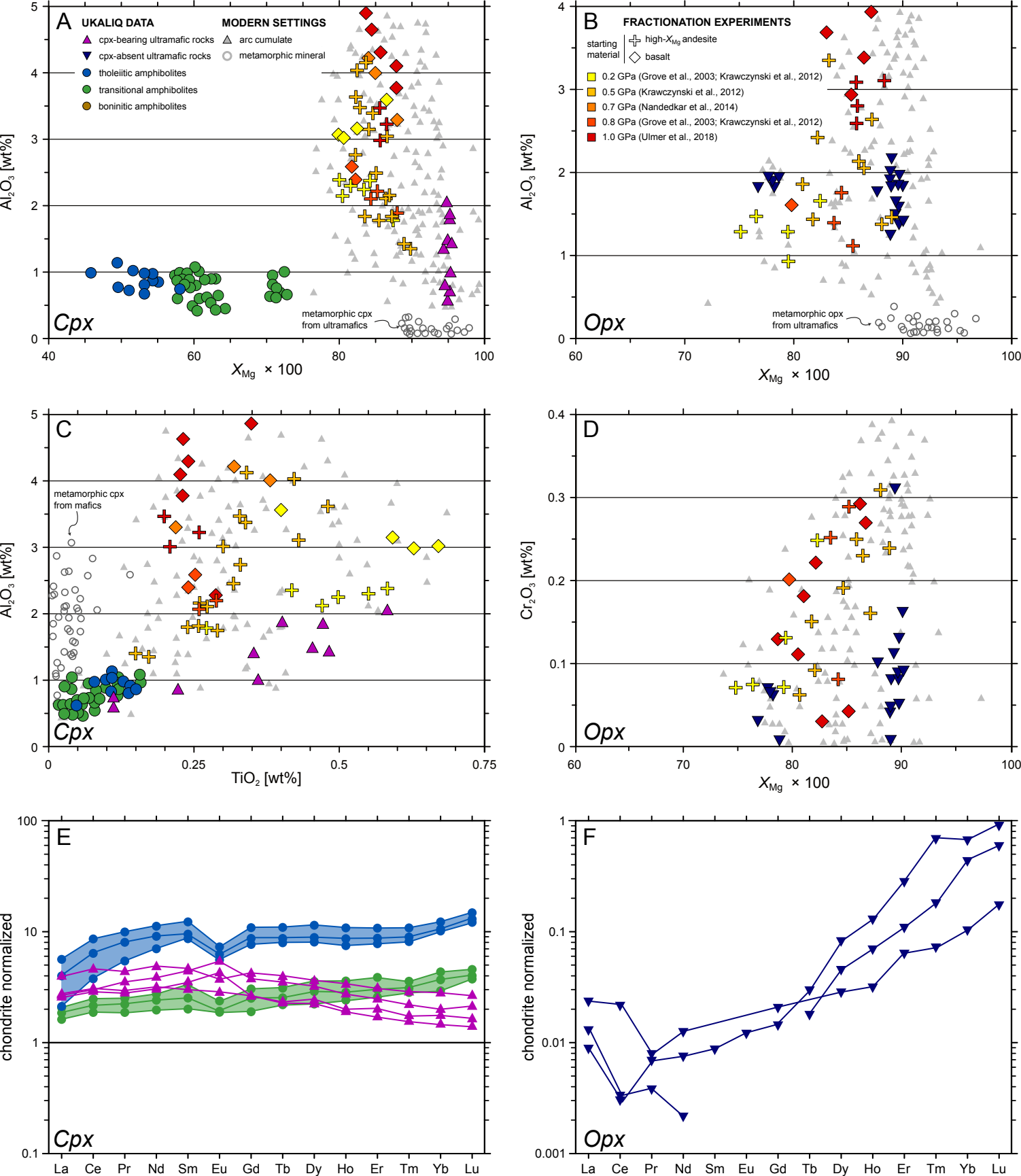
A
UKALIQ DATA
cpx-bearing ultramafic rocks
cpx-absent ultramafic rocks
tholeiitic amphibolites
transitional amphibolites
boninitic amphibolites
MODERN SETTINGS
arc cumulate
metamorphic mineral
Cpx
metamorphic cpx
from ultramafics
Al2O3 [wt%]
XMg × 100
B
FRACTIONATION EXPERIMENTS
starting material
high-XMg andesite
basalt
0.2 GPa (Grove et al., 2003; Krawczynski et al., 2012)
0.5 GPa (Krawczynski et al., 2012)
0.7 GPa (Nandedkar et al., 2014)
0.8 GPa (Grove et al., 2003; Krawczynski et al., 2012)
1.0 GPa (Ulmer et al., 2018)
Opx
metamorphic opx
from ultramafics
C
metamorphic cpx
from mafics
TiO2 [wt%]
D
Cr2O3 [wt%]
E
chondrite normalized
La Ce Pr Nd Sm Eu Gd Tb Dy Ho Er Tm Yb Lu
F

Figure 7.

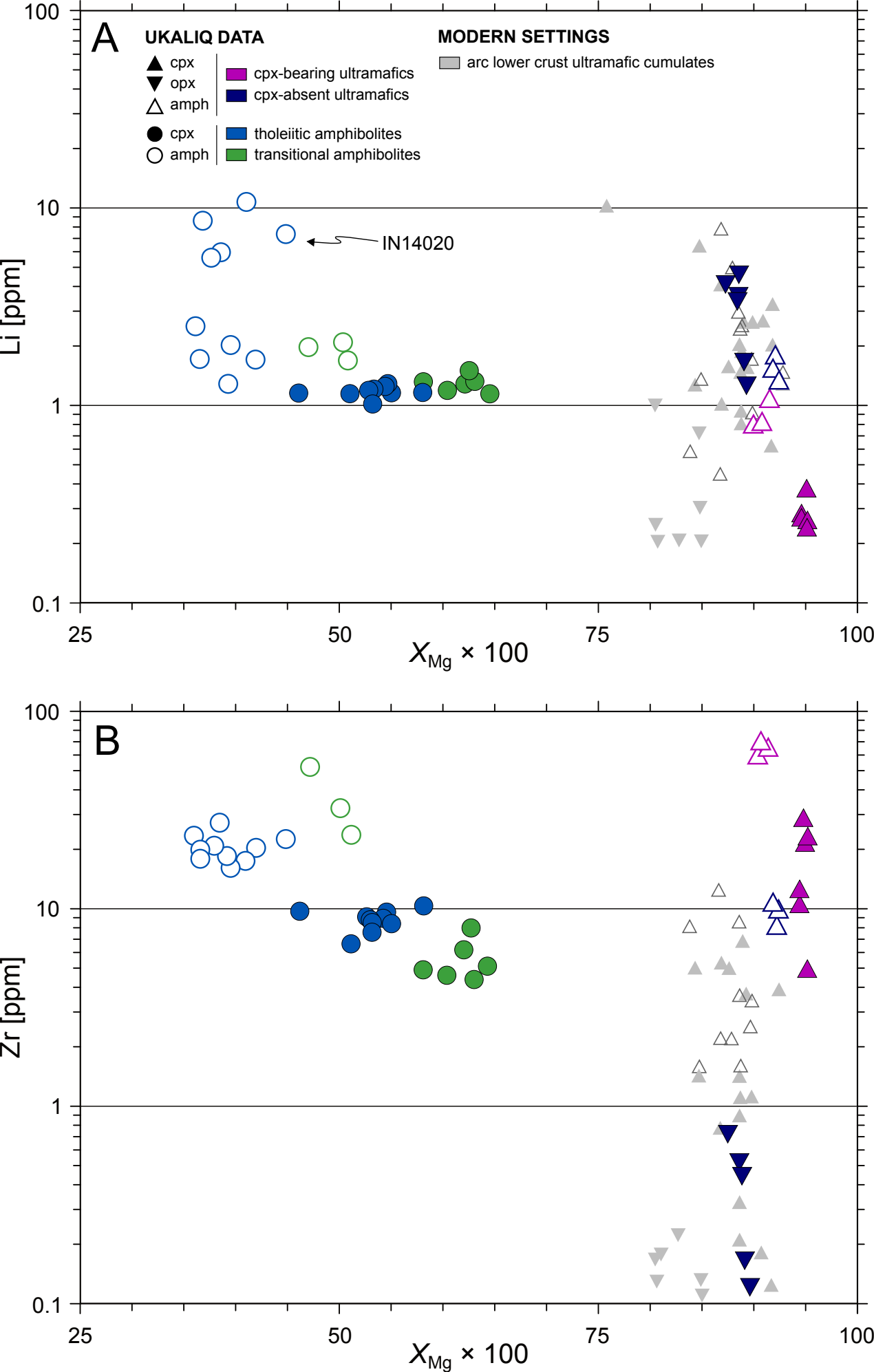
A
UKALIQ DATA
cpx
opx
amph
cpx-bearing ultramafics
cpx-absent ultramafics
cpx
amph
tholeiitic amphibolites
transitional amphibolites
MODERN SETTINGS
arc lower crust ultramafic cumulates
IN14020
Li [ppm]
100
10
1
0.1
25
50
75
100
X_{Mg} × 100
B
Zr [ppm]
100
10
1
0.1
25
50
75
100
X_{Mg} × 100

Figure 8.

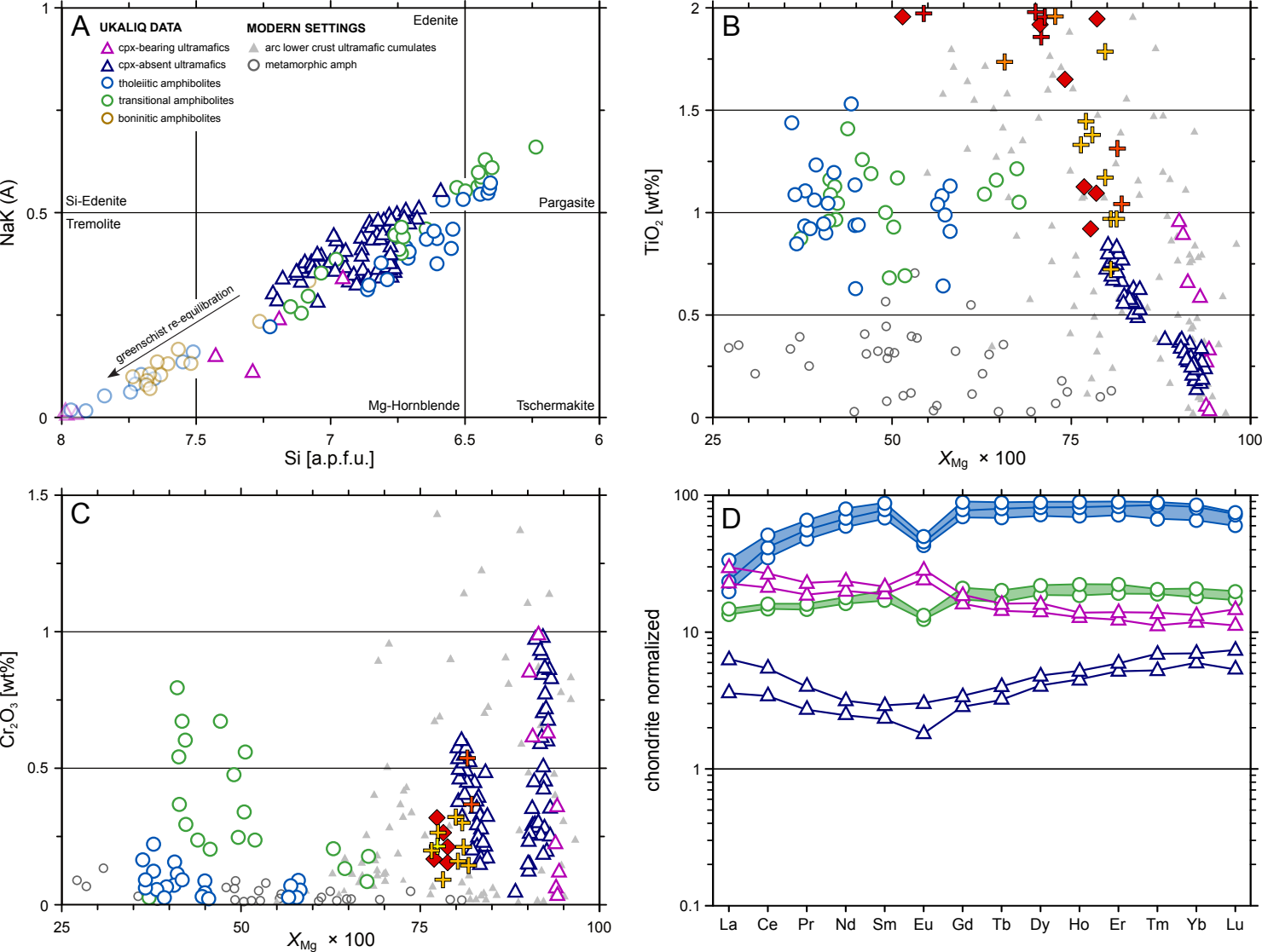
A
UKALIQ DATA
cpx-bearing ultramafics
cpx-absent ultramafics
tholeiitic amphibolites
transitional amphibolites
boninitic amphibolites
MODERN SETTINGS
arc lower crust ultramafic cumulates
metamorphic amph
Edenite
Si-Edenite
Pargasite
Tremolite
Mg-Hornblende
Tschermakite
greenschist re-equilibration
NaK (A)
Si [a.p.f.u.]
B
TiO2 [wt%]
XMg × 100
C
Cr2O3 [wt%]
XMg × 100
D
chondrite normalized
La Ce Pr Nd Sm Eu Gd Tb Dy Ho Er Tm Yb Lu

Figure 9.

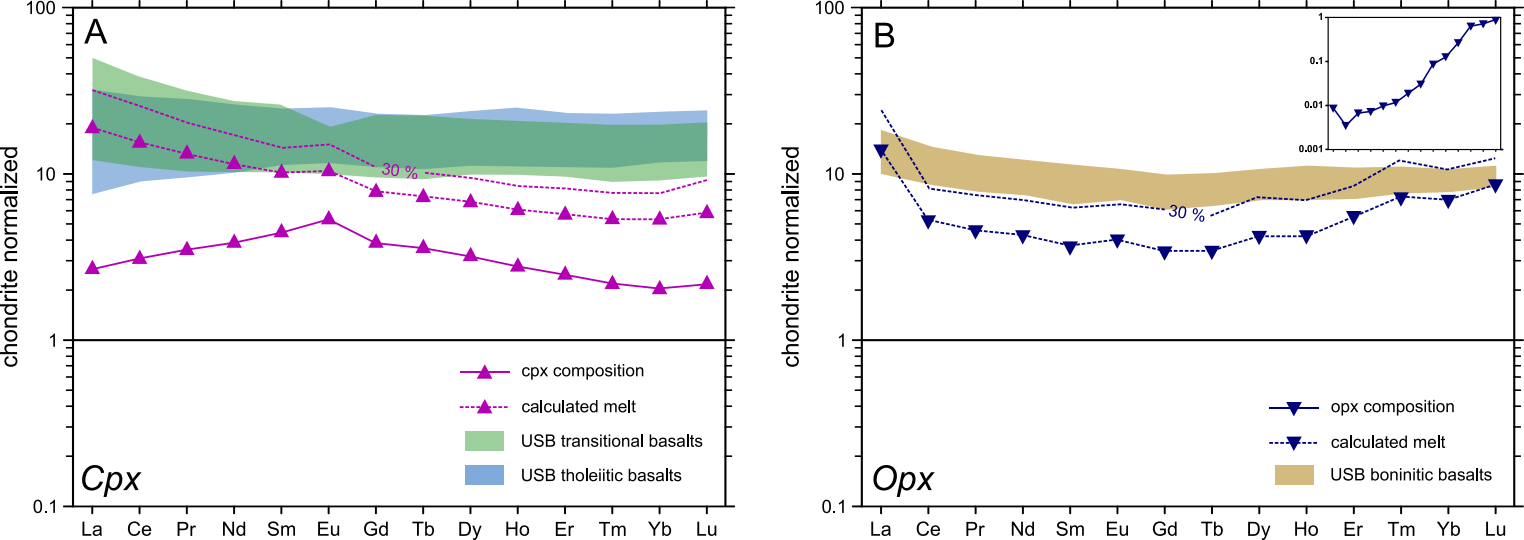
A
B
chondrite normalized
100
10
1
0.1
30 %
cpx composition
calculated melt
USB transitional basalts
USB tholeiitic basalts
Cpx
opx composition
calculated melt
USB boninitic basalts
Opx
La
Ce
Pr
Nd
Sm
Eu
Gd
Tb
Dy
Ho
Er
Tm
Yb
Lu

Figure 10.

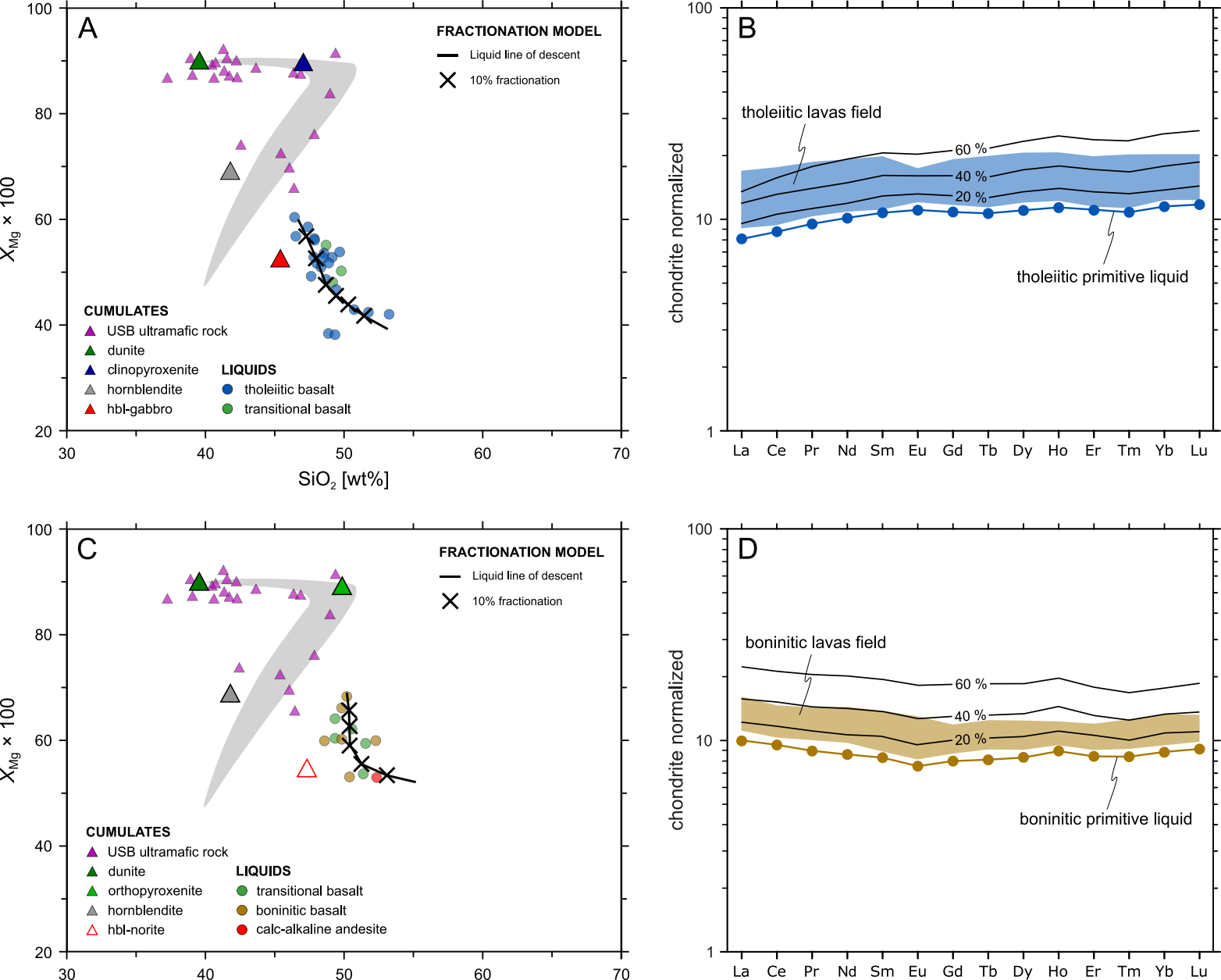
A
FRACTIONATION MODEL
Liquid line of descent
10% fractionation
CUMULATES
USB ultramafic rock
dunite
clinopyroxenite
hornblendite
hbl-gabbro
LIQUIDS
tholeiitic basalt
transitional basalt
X_{Mg} × 100
SiO_2 [wt%]
B
tholeiitic lavas field
60 %
40 %
20 %
tholeiitic primitive liquid
chondrite normalized
La Ce Pr Nd Sm Eu Gd Tb Dy Ho Er Tm Yb Lu
C
FRACTIONATION MODEL
Liquid line of descent
10% fractionation
CUMULATES
USB ultramafic rock
dunite
orthopyroxenite
hornblendite
hbl-norite
LIQUIDS
transitional basalt
boninitic basalt
calc-alkaline andesite
X_{Mg} × 100
D
boninitic lavas field
60 %
40 %
20 %
boninitic primitive liquid
chondrite normalized
La Ce Pr Nd Sm Eu Gd Tb Dy Ho Er Tm Yb Lu

Figure 11.

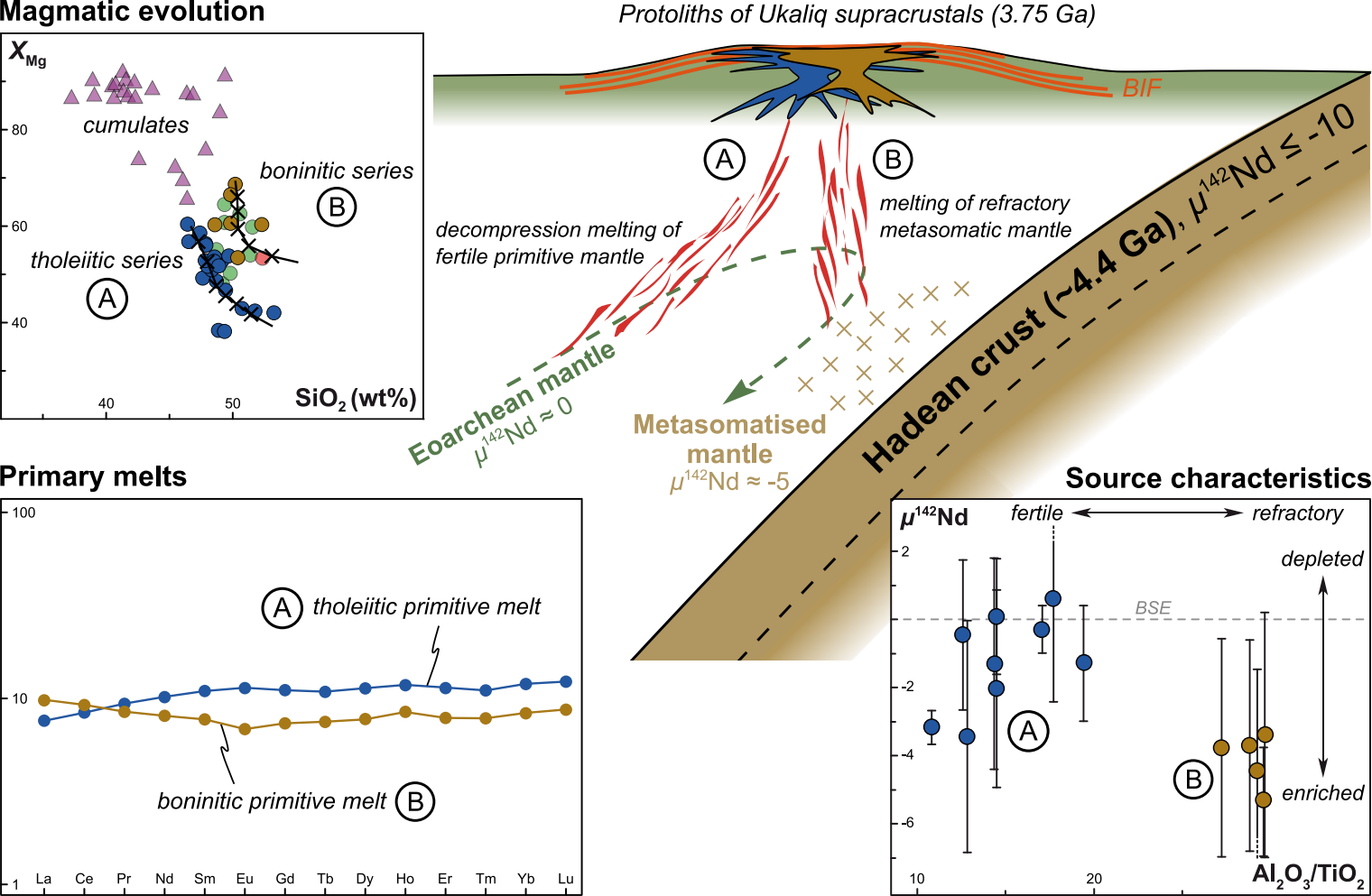
Magmatic evolution
X_{Mg}
80
60
40
cumulates
boninitic series
B
tholeiitic series
A
40
50
SiO_2 (wt%)
Protoliths of Ukaliq supracrustals (3.75 Ga)
BIF
A
B
melting of refractory metasomatic mantle
decompression melting of fertile primitive mantle
Eoarchean mantle
$\mu^{142}Nd \approx 0$
Metasomatised mantle
$\mu^{142}Nd \approx -5$
Hadean crust (~4.4 Ga), $\mu^{142}Nd \leq -10$
Primary melts
100
10
1
A tholeiitic primitive melt
boninitic primitive melt B
La Ce Pr Nd Sm Eu Gd Tb Dy Ho Er Tm Yb Lu
Source characteristics
$\mu^{142}Nd$
fertile
refractory
depleted
enriched
BSE
2
-2
-4
-6
A
B
10
20
Al_2O_3/TiO_2